Computer Methods in Applied Mechanics and Engineering 418 (2024) 116492

Contents lists available at ScienceDirect

Comput. Methods Appl. Mech. Engrg.

journal homepage: www.elsevier.com/locate/cma

Empirical Interscale Finite Element Method (EIFEM) for modeling heterogeneous structures via localized hyperreduction

J.A. Hernández [a,c], A. Giuliodori [a,b,*], E. Soudah [a,d]

[a] Centre Internacional de Mètodes Numèrics en Enginyeria (CIMNE), Barcelona, Spain
[b] Universitat Politècnica de Catalunya, BarcelonaTech (UPC), Barcelona, Spain
[c] E.S. d'Enginyeries Industrial, Aeroespacial i Audiovisual de Terrassa, Technical University of Catalonia, C/ Colom, 11, Terrassa 08222, Spain
[d] Mechanical Engineering Department, Faculty of Industrial Engineering of the University of Valladolid, 47011 Valladolid, Spain

ARTICLE INFO

Keywords:
Multiscale FEM
Hyperreduction
Empirical cubature
ROM
FEM

ABSTRACT

This work proposes a special type of Finite Element (FE) technology – the *Empirical Interscale FE method* – for modeling heterogeneous structures in the small strain regime, for both dynamic and static analyses. The method combines a domain decomposition framework, where interface conditions are established through "fictitious" frames, with dimensional hyperreduction at subdomain level. Similar to other multiscale FE methods, the structure is assumed to be partitioned into coarse-scale elements, each of these elements is equipped with a fine-scale subgrid, and the displacements of the boundaries of the coarse-scale elements are described by standard polynomial FE shape functions. The distinguishing feature of the proposed method is the employed "interscale" variational formulation, which directly relates coarse-scale nodal internal forces with fine-scale stresses, thereby avoiding the typical nested local/global problems that appear, in the nonlinear regime, in other multiscale methods. This distinctive feature, along with hyperreduction schemes for nodal internal and external body forces , greatly facilitate the implementation of the proposed formulation in existing FE codes for solid elements. Indeed, one only has to change the location and weights of the integration points, and to replace a few polynomial-based FE matrices with "empirical" operators, i.e., derived from the information obtained in appropriately chosen computational experiments. We demonstrate that the elements resulting from this formulation are not afflicted by volumetric locking when dealing with nearly-incompressible materials, and that they can handle non-matching fine-scale grids as well as curved structures. Last but not least, we show that, for periodic structures, this method converges upon mesh refinement to the solution delivered by classical first-order computational homogenization. Thus, although the method does not presuppose scale separation, it can represent solutions in this limiting case by taking sufficiently small coarse-scale elements.

1. Introduction

In recent years, several multiscale techniques based on the finite element (FE) method have been developed to address the challenges associated with modeling structures exhibiting significant material and geometric variations at different length scales—see e.g. the review in Ref. [1]. The present paper introduces yet another variant of these techniques: the *Empirical Interscale Finite Element Method* (EIFEM). As we argue in the ensuing discussion, we have chosen the qualifiers *empirical* and *interscale* to highlight

* Corresponding author at: Universitat Politècnica de Catalunya, BarcelonaTech (UPC), Barcelona, Spain.
E-mail address: agustina.giuliodori@upc.edu (A. Giuliodori).

https://doi.org/10.1016/j.cma.2023.116492
Received 9 June 2023; Received in revised form 11 August 2023; Accepted 26 September 2023
Available online 4 October 2023
0045-7825/© 2023 The Authors. Published by Elsevier B.V. This is an open access article under the CC BY license (http://creativecommons.org/licenses/by/4.0/).

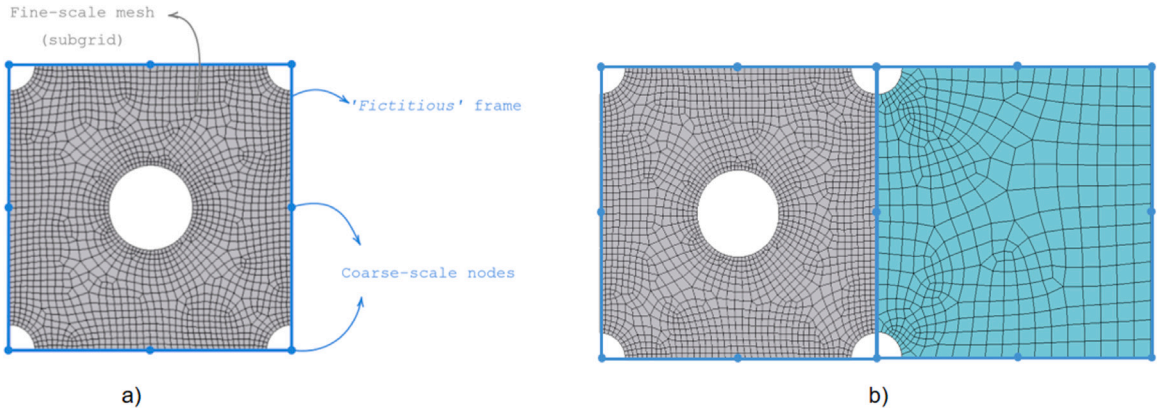

Fig. 1. (a) Coarse-scale quadratic element corresponding to a porous unit cell, along with the associated fine-scale mesh. The boundary of the element is to be regarded as a "fictitious" frame, in the sense that some of the points of such boundary does not coincide with any material point. For instance, in this case, the coarse-scale corner nodes are not material points. (b) Coarse-scale mesh with associated (non-matching) fine grids of a given structure made of two distinct types of quadratic elements.

the major differences of the proposed method with respect to the standard Finite Element Method (FEM) and other existing FE-based multiscale techniques.

Similar to other FE-based methods, such as the multiscale FEM [2], in the EIFEM, the structure under study is divided into coarse-scale elements, and each of these elements is assumed to contain a fine-scale mesh able to capture the heterogeneous nature of the structure at the desired level of accuracy. The boundary of each coarse-scale element is to be regarded as a fictitious one, in the sense that some points of such boundary may not correspond to any material point; this consideration is depicted in Fig. 1.a. The displacement of this coarse-scale fictitious boundary is described by standard polynomial FE shape functions. Curved elements can be modeled by using quadratic shape functions (or any other higher order); furthermore, the fine-scale meshes associated to contiguous coarse-scale elements may be non-matching (as illustrated in Fig. 1.b).

Likewise, similar to FE schemes based on computational homogenization (such as the so-called FE^2 method [3]), the proposed EIFEM employs strain and stress measures at both scales. The stresses and strains at the fine-scale partition are the standard Cauchy stresses and infinitesimal strains of classical continuum theories. The coarse-scale strains and stresses, on the other hand, are low dimensional parameterizations of fine-scale nodal deformational displacements and nodal interdomain forces. The distinguishing feature of the proposed EIFEM is the use of a multiscale variational framework in which *coarse-scale internal forces are linked directly to fine-scale (Cauchy) stresses* —this is why we call the method interscale in the first place. We will see that this attribute allows one to easily implement this method in existing FE codes, for it precludes the need of solving nested boundary value problems, as it occurs in computational homogenization problems addressed by the so-called FE^2 method [3], or in their reduced-order model (ROM) variants [4–7].

On the other hand, we use the appellation empirical to refer to the fact that the typical ingredients for determining the (coarse-scale) nodal forces of a given element are not derived directly from the polynomial shape functions chosen for describing the displacements of the boundary of the element, but rather are computed from solutions obtained in appropriately chosen computational experiments. More specifically, the low-dimensional parameterizations alluded to earlier are modal expansions in which the modes are computed as the left singular vectors of the Singular Value Decomposition (SVD) of the solutions obtained in such tests.

The other ingredient in the proposed EIFEM which is empirically derived is the multidimensional quadrature (or cubature rule) for integrating internal and body forces. Indeed, the displacements of the boundary of the coarse-scale elements are described by polynomial shape functions, and thus, the integrals associated to boundary terms (say surface traction) can be accurately approximated by the same Gaussian rules used in the standard FEM. By contrast, the volumetric integrals involved in evaluation of coarse-scale nodal forces (including inertial terms) cannot be evaluated using Gaussian rules, because such rules presume that the integrand is amenable to accurate approximation by (globally supported) polynomial functions in regular polyhedron—which is clearly not the case. Of course one can always resort to the elemental Gaussian rules used for integrating internal forces and external forces in the fine-scale mesh. However, this choice would render the method impractical, because the total number of integration would scale with the complexity of the fine-scale mesh.

To address this issue and introduce *hyperreduction* (i.e., an additional reduction in complexity aside from the one obtained by the low-dimensional modal expansions), we have adapted to the problem under consideration the algorithm recently proposed by the first author and collaborators in Ref. [8], called the *Continuous Empirical Cubature Method* (CECM). The appellation empirical here has the same connotation that in the EIFEM: the method has been devised to numerically approximate the integral of functions obtained in computational experiments (FE tests), in which the only information available about the integrand is their values at the Gauss points of the underlying mesh. The qualifier continuous, on the other hand, refers to the fact that the objective function (which is the integration error) in the associated optimization problem depends continually on the position of the integration points,

and therefore such points may occupy any position within the domain. This is contrast to other cubature methods advocated in the related literature, which may be seen as discrete cubature methods, for the integration points are selected among the Gauss points of the underlying finite element grid. This is the case of the technique put forward by the first author in Refs. [9,10], the quadrature scheme based on linear programming proposed by A. Patera and co-workers [11–13], and the Energy-Conserving Mesh Sampling and Weighting (ECSW) scheme advocated by C. Farhat and co-workers [14] (in the latter case, one selects elements, rather than Gauss points).

1.1. Scope and related works

We will focus solely on the derivation of the interscale operators for solid elements. Likewise, the formulation presented here is only valid for small strains, for it relies on the kinematic decomposition of fine-scale displacements into infinitesimal rigid body displacements and deformational displacements. By contrast, we place no constraints on the type of constitutive equations the method can handle. In fact, we will see that, even if the domain is trained in the elastic regime, the resulting element may be applied to analyze nonlinear material behavior (subject to certain caveats). The same applies to dynamical analysis: even if one trains the element in the static regime, the resulting formulation may be used in dynamical problems as well.

The method proposed in the present work may be deemed as the generalization to arbitrarily shaped structures of the hyperreduced-order domain decomposition method proposed by the authors in Refs. [10,15]. In turn, these two works draw upon the variational partitioning scheme advocated by Park and Felippa in Ref. [16] —known as the Localized Lagrange Multipliers method. The major innovative features of the present paper with respect to the former two works are the listed below.

1. As already pointed out, the proposed method does not require the fine-scale discretization of contiguous elements to be conforming. This brings a significant advantage with respect to Refs. [10,15] (in which fine-scale matching grids are a prerequisite), because it allows us to train a given parent domain without regard of which will be the elements potentially in contact with it.
2. In Refs. [10,15], interface boundaries are required to be non-intersecting planar surfaces. There is no such a restriction in the method proposed here.
3. In Refs. [10,15], the coarse-scale kinematic is dictated by the type of tests employed to train the model: the basic displacement interface parameterization is assumed always to be linear, and additional local interface modes are inferred from the training tests by exploiting the notion of subspace intersection (this is actually why the fine-scale grids in Refs. [10,15] are to be compatible). In the interest of generality and versatility, more aligned with the spirit of standard FE approaches, we take here the reverse route: rather than proposing a set of training tests, and then infer the kinematics, here it is the user who proposes the coarse-scale kinematics (linear, quadratic, etc...), and then the training tests are tailored to this very choice.
4. While both Refs. [10,15] exploit the concept of empirical cubature of internal forces, the method employed therein is of discrete nature, that is, the reduced set of integration points is selected among the Gauss points of the underlying mesh. By contrast, as already noted, in the present work, in order to increase the efficiency of the integration (same accuracy for less integration points), the integration points may take any position within the domain.
5. Both Refs. [10,15] deals with quasi-static problems. Here we extend the formulation to embrace dynamical problems as well.

Considered in a wider context, the EIFEM belongs to the class of general multiscale approaches for the approximation of the solution of problems with complex heterogeneities and large domains (an extensive review of such approaches is given in Ref. [2]). Among all these methods, our work bears some resemblance to the General Multiscale Finite Element Method (GMsFEM) presented in Ref. [17] and related works (see, for instance, Refs. [18–21]), in which multiscale FE basis functions are built for capturing the small scale information within each coarse element [18]. The EIFEM also exhibits features akin to the multiscale method recently proposed in Ref. [22], since it combines the variational multiscale method (see Ref. [23]), with domain decomposition and Model Order Reduction (MOR) techniques. As in our proposal, such approaches pre-compute multiscale local basis functions in an offline stage in order to enrich the global solution at the coarse level. However, all these methods need to integrate the resulting equations in all the fine-grid integration points, a fact that invariably restricts their scope to linear problems. It should be remarked that, thanks to the offline derivation of efficient integration rules, our approach is valid when material non-linearities are present, and our online computational cost depends only on the number of coarse-scale integration points (yet not on the complexity of the underlying finite element discretization).

2. Training stage

Attention is focused first on the design of the FE tests used to "train" the *Empirical Interscale Finite Element* (EIFE) model. The particular domain chosen for carrying out the FE tests will be hereafter termed the *EIFE parent domain* of this type of coarse-scale element.

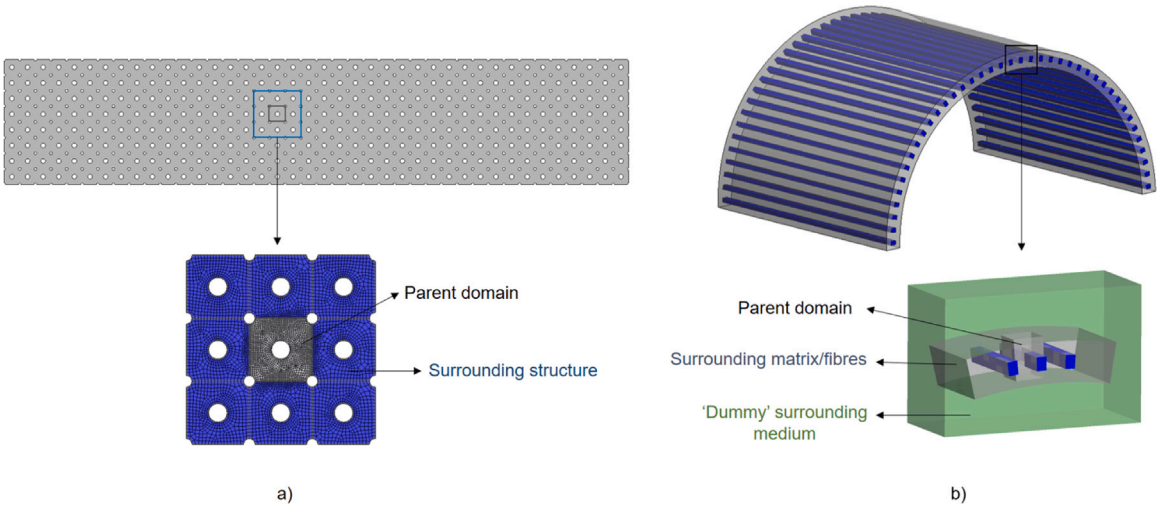

Fig. 2. Oversampling technique. (a) Periodic structure. The training domain consists of a 3×3 sample of porous unit cells; the EIFE parent domain is the cell in the centre, which is meshed with a finer grid than the rest. (b) Curved structured. In this case, the EIFE parent domain is a curved heterogeneous hexahedra (matrix + reinforcement), and the training domain is formed by this parent domain together to cells of the same type in the circumferential and axial direction, and a "dummy" surrounding structure whose elastic properties may be taken equal to that of the matrix material.

2.1. Training domain and boundary conditions

In regards to the imposition of boundary conditions for training the domain, we adopt the *oversampling* method proposed by Hou et al. [18] in the context of the multiscale finite element method—also employed by the authors in Refs. [10,15]. In this method, the domain whose coarse-scale model is to be constructed is embedded in a larger domain (see Fig. 2), and it is on the boundary of this larger domain that the conditions are imposed. We will refer to this larger domain as the training domain.

The composition of the structure in which the parent domain is embedded should be representative of what one would encounter in a practical scenario. For instance, if the domain is a unit cell of a periodic structure, then the logical choice is to surround the domain by other unit cells, as shown in Fig. 2.a. Likewise, in curved structures such as the one shown in Fig. 2.b, in which the studied domain is not expected to be surrounded by any material in the radial direction, one may fill the training domain by a "dummy" material. As for the size of the training domain, numerical experience indicates that coarse-scale elements obtained with training domains with characteristic lengths above 3 times larger than the characteristic length of the parent domain are practically the same in terms of stiffness. This implies that, for instance, in periodic structures such as the one shown in Fig. 2.a, it suffices to take a training domain containing 3×3 unit cells. The spatial discretization of the surrounding medium may be taken of lower resolution than that of the parent domain.

2.2. Basic training tests

Let n denote the number of degrees of freedom (DOFs) of the coarse-scale element (equal to the number of nodes n^{nod} times the spatial dimension of the problem $d = 2, 3$). At the very least, the training should include a set of n tests in the linear elastic range in which displacements on the external boundary are imposed according to the employed shape functions. We will call these tests the *basic training tests*. This is illustrated in Fig. 3, where we display the deformed shapes corresponding to the $n = 4 \cdot 2 = 8$ basic training tests used for deriving an EIF linear quadrilateral element for the unit cell shown previously in Fig. 2.a. Aside from the above mentioned basic tests, one may include additional tests featuring different boundary conditions and/or material parameter variations, conducted in either the linear or nonlinear range. Nevertheless, it should be stressed that, when determining the characteristic modes of the domain, priority should be given to the data obtained in the basic tests—in the sense that the subspace spanned by the solution snapshots corresponding to these tests should be contained in the subspace spanned by the characteristic modes.

2.3. Snapshots matrices

The data required from the training tests for the construction of the EIFE operators are, on the one hand, the variables defining the mesh of the studied domain (coordinates, element connectivity, boundary nodes, type of finite element, etc.), and, on the other hand, the vectors of nodal displacements, nodal interface forces, and stresses for each of the tests. These three variables are stored in snapshot matrices $\boldsymbol{A}_d$, $\boldsymbol{A}_\lambda$ and $\boldsymbol{A}_\sigma$, respectively. The size of the displacement snapshot matrix $\boldsymbol{A}_d$ is $N \times P$, where N denotes the total number of DOFs of the fine-scale mesh, whereas P designates the total number of displacement solutions (or "snapshots") for

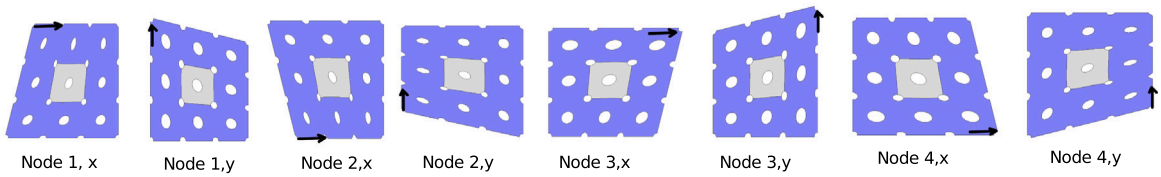

Fig. 3. Deformed shapes corresponding to the basic training test required for deriving a 4-node quadrilateral EIFE for the unit cell shown previously in Fig. 2.a. In each test, displacement conditions corresponding to linear shape functions are prescribed. The tests are carried out in the linear elastic range.

all time steps and tests. When only basic training tests are used, then the number of snapshots is equal to the number of coarse-scale DOFs ($P = n$).

What we call here nodal interface forces are the forces exerted by the remaining structure upon the studied domain. These forces are only nonzero on the interface boundary nodes, and therefore, the size of the snapshot matrix $\boldsymbol{A}_\lambda$ is $M \times P$, M being the number of DOFs of the interface boundary. It should be noticed that, when using basic training tests, since there are not external forces and the problem is linear, $\boldsymbol{A}_\lambda$ may be simply obtained by multiplying the stiffness matrix of the domain times the displacement snapshot matrix $\boldsymbol{A}_d$. On the other hand, each column of $\boldsymbol{A}_\sigma$ contains the vector of Cauchy stress $\boldsymbol{\sigma} \in \mathbb{R}^s$ ($s = 4$ for plane strain and $s = 6$ for 3D problems) at all the points of the discretization. Thus, the size of $\boldsymbol{A}_\sigma$ is $sG \times P$, G being the total number of Gauss points of the fine-scale mesh.

3. Modal approximations of fine-scale variables

The recipe followed in the ensuing discussion to derive the EIFE formulation is, in essence, the same used by the authors in Ref. [15] for prismatic structures, namely: introducing modal approximations for the fine-scale variables, and then determining the stationary points of a three-field energy functional involving such modal approximations. The major difference is that here we strive to give a multiscale interpretation to each of the steps of the procedure, in contrast to Ref. [15], wherein the methodology is simply presented as a specific instance of domain decomposition combined with reduced-order modeling. The purpose of introducing this multiscale interpretation is to reveal the differences between the proposed approach and reduced-order methods (such as those presented in Refs. [5–7]) based on the classical axiomatic framework of computational homogenization (which rests on the notion of equilibrium of a RVE and the Hill–Mandel Principle of Macro-Homogeneity, among others ingredients).

It should be noted that the EIF operators presented in the following are referred to a single parent domain, and are expressed in a reference system intrinsic to this domain. The extension to EIF elements of arbitrary size and orientation will be addressed in Section 4.5 and Appendix B.

Remark 3.1. For the sake of notational simplicity, in what follows, all variables will be referred to a specific parent domain, without any reference to the global assembly of EIF elements. Besides, when the same variable is defined at both scales, we will use superscripts "μ" and "c" to distinguish fine-scale and coarse-scale variables, respectively, except for those cases in which the variable appears in the final formulation, in which bare symbols will be employed instead. Accordingly, the vectors of coarse-scale nodal displacements and fine-scale strains and stresses, which do appear in the final formulation (that is why the method is dubbed interscale) will be denoted by $\boldsymbol{d}$, $\boldsymbol{\epsilon}$ and $\boldsymbol{\sigma}$, respectively, whereas fine-scale displacements, coarse-scale stresses and coarse-scale strains, which do not appear in the final formulation, will be designated by $\boldsymbol{d}^\mu$, $\boldsymbol{\sigma}^c$ and $\boldsymbol{\epsilon}^c$, respectively.

3.1. Approximation of displacements: generalized coarse-scale strains

The proposed modal approximation for the fine-scale nodal displacement $\boldsymbol{d}^\mu$ adopts the form

$$\boldsymbol{d}^\mu = \boldsymbol{R}\boldsymbol{a} + \boldsymbol{\Phi}\boldsymbol{\epsilon}^c. \tag{1}$$

Here, $\boldsymbol{R} \in \mathbb{R}^{N \times n^{rb}}$ denotes the matrix of rigid body modes of the domain ($n^{rb} = 3$ or $n^{rb} = 6$ for 2D or 3D problems, respectively), whereas $\boldsymbol{\Phi} \in \mathbb{R}^{N \times p}$ stands for the matrix of deformational modes; $\boldsymbol{a} \in \mathbb{R}^{n^{rb}}$ and $\boldsymbol{\epsilon}^c \in \mathbb{R}^p$, on the other hand, are the corresponding amplitude vectors. Rigid body and deformational modes are assumed to be orthogonal in the inner product induced by the geometric mass matrix of the domain $\boldsymbol{M}^\mu$:

$$\boldsymbol{R}^T \boldsymbol{M}^\mu \boldsymbol{\Phi} = \boldsymbol{0}. \tag{2}$$

The geometric mass matrix $\boldsymbol{M}^\mu$ is constructed as the standard FE mass matrix, but with density equal to one, that is

$$\boldsymbol{M}^\mu := \int_\Omega \boldsymbol{N}^{\mu T} \boldsymbol{N}^\mu \, d\Omega, \tag{3}$$

$\boldsymbol{N}^\mu : \Omega \to \mathbb{R}^{d \times N}$ being the matrix of fine-scale shape functions (in its globally supported format). The condition of $\boldsymbol{M}^\mu$-orthogonality is also imposed, column-wise, to the deformational modes:

$$\boldsymbol{\Phi}^T \boldsymbol{M}^\mu \boldsymbol{\Phi} = \boldsymbol{I} \tag{4}$$

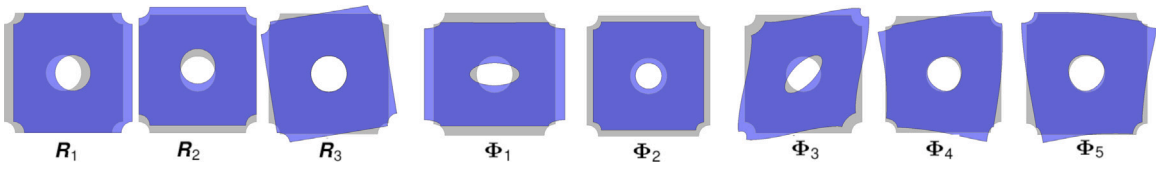

Fig. 4. Deformed shapes of the rigid body modes $\boldsymbol{R}$ and deformational modes $\boldsymbol{\Phi}$ corresponding to the displacement snapshots built with data of the training tests shown in Fig. 3. The amplitude of the latter modes play the role of generalized coarse-scale strains in our formulation.

(here $\boldsymbol{I}$ stands for the $p \times p$ identity matrix). The deformational modes $\boldsymbol{\Phi}$ are computed from the snapshot matrix of displacements $\boldsymbol{A_d}$ by first determining the deformational component of such a matrix (in order to meet orthogonality condition (2)):

$$\widetilde{\boldsymbol{A_d}} = \boldsymbol{A_d} - \boldsymbol{R}(\boldsymbol{R}^T \boldsymbol{M}^{\mu} \boldsymbol{R})^{-1} \boldsymbol{R}^T \boldsymbol{M}^{\mu} \boldsymbol{A_d}, \tag{5}$$

and then, in order to meet orthogonality condition (4), and also filter out undesirable noisy modes, determine $\boldsymbol{\Phi}$ as the left-singular vectors of the weighted Singular Value Decomposition (WSVD) of $\widetilde{\boldsymbol{A_d}}$ (see Algorithm 1 in page 11 of Ref. [15]):

$$[\boldsymbol{\Phi}, \boldsymbol{S}_d, \boldsymbol{V}_d] \leftarrow \texttt{WSVD}(\widetilde{\boldsymbol{A_d}}, \boldsymbol{M}^{\mu}, \epsilon_d) \tag{6}$$

Here $0 \leq \epsilon_d < 1$ is a relative truncation threshold, whereas $\boldsymbol{S}_d$ and $\boldsymbol{V}_d$ denote the matrices of singular values and right-singular vectors, respectively.

Fig. 4 displays the deformed shapes of the $n^{rb} = 3$ rigid body modes and $p = 5$ deformational modes obtained from the $n = 8$ displacement snapshots determined from the tests displayed in Fig. 3. The origin of coordinates is taken as the centroid of the domain; thus, a_3 represents the amplitude of an (infinitesimal) rotation around the axis passing through the centroid (and a_1 and a_2 translations along the reference axes). On the other hand, the role of *generalized coarse-scale strains* is assigned to the amplitudes of the deformational modes (hence the notation $\boldsymbol{\varepsilon}^c$), on the grounds that they represent a low-dimensional parametrization of the deformational state of the domain. It follows then that the number of coarse-scale strains in our formulation is dictated by the order of interpolation of the coarse-scale element. The rule is that

$$p = \texttt{ncol}(\boldsymbol{\Phi}) \geq n - n^{rb} \tag{7}$$

($\texttt{ncol}(\boldsymbol{\Phi})$ stands for the number of columns of $\boldsymbol{\Phi}$). Thus, for a quadratic quadrilateral EIF element, $p \geq 13$, whereas for a quadratic hexahedra, $p \geq 72$. Note that this is in stark contrast to standard (first-order) homogenization methods, in which the number of coarse-scale strains is the same regardless of the employed coarse-scale FE elements (3 for plane strains and 6 for 3D problems).

3.2. Approximation of interface forces: generalized coarse-scale stresses

In first-order homogenization procedures (see e.g. Ref. [24]), the coarse-scale (Cauchy) stress tensor is determined either by volume averaging of fine-scale stresses, or equivalently, as the integral of an expression involving the surface tractions at the external boundary of the RVE. According to the latter approach, the coarse-scale stress tensor may be viewed as a low-dimensional parametrization of the surface tractions at the RVE boundary. In the following discussion, we adopt this very interpretation to define the *generalized coarse-scale stresses* of our formulation.

Let $\lambda \in \mathbb{R}^M$ denote the forces at the interface boundary nodes of the domain (these forces are the nodal projection of the above mentioned surface tractions). Without loss of generality, we may write λ in terms of the vector of generalized coarse-scale stresses $\boldsymbol{\sigma}^c$ as follows:

$$\lambda = \widehat{\boldsymbol{\Psi}} \boldsymbol{r} + \boldsymbol{\Psi} \boldsymbol{\sigma}^c. \tag{8}$$

Here, $\widehat{\boldsymbol{\Psi}}$ and $\boldsymbol{\Psi}$ are mutually orthogonal matrices (in a sense that will be defined later), whereas $\boldsymbol{r}$ is the amplitude vector for $\widehat{\boldsymbol{\Psi}}$. It can be argued that, in order for $\boldsymbol{\sigma}^c$ to qualify as a valid stress measure, the work done by the component $\boldsymbol{\Psi}\boldsymbol{\sigma}^c$ in Eq. (8) upon rigid body displacements must be zero. This leads to the condition

$$\boldsymbol{R}_{\boldsymbol{b}}^T \boldsymbol{\Psi} = \boldsymbol{0}, \tag{9}$$

where $\boldsymbol{R}_{\boldsymbol{b}} \in \mathbb{R}^{M \times n^{rb}}$ is the sub-matrix of the rigid body modes $\boldsymbol{R}$ formed by the rows of the interface boundary DOFs $\boldsymbol{b} \in \{1, 2 \dots N\}$ ($\boldsymbol{R} = \boldsymbol{R}(\boldsymbol{b}, :)$ in the so-called "colon" notation [25]). It can be readily seen that the preceding condition amounts to stating that the resultants and moment resultants of each of the columns of $\boldsymbol{\Psi}$ are zero—for this reason, hereafter we will refer to $\boldsymbol{\Psi}$ as the matrix of self-equilibrated modes.

Let us now determine an expression for $\widehat{\boldsymbol{\Psi}}$ by imposing that $\widehat{\boldsymbol{\Psi}}$ and $\boldsymbol{\Psi}$ are mutually orthogonal. As the authors demonstrate in Ref. [15], Appendix A, L_2-orthogonality of surface tractions on the interface boundary translates into $\bar{\boldsymbol{M}}^{-1}$-orthogonality of the corresponding nodal interface forces, $\bar{\boldsymbol{M}} \in \mathbb{R}^{M \times M}$ being the geometric mass matrix of the interface boundary. Thus, if we use this $\bar{\boldsymbol{M}}^{-1}$-orthogonality, we get that $\widehat{\boldsymbol{\Psi}}^T \bar{\boldsymbol{M}}^{-1} \boldsymbol{\Psi} = \boldsymbol{0}$. Comparison of this expression with Eq. (9) reveals that the expression for the desired matrix is

$$\widehat{\boldsymbol{\Psi}} := \bar{\boldsymbol{M}} \boldsymbol{R}_{\boldsymbol{b}}. \tag{10}$$

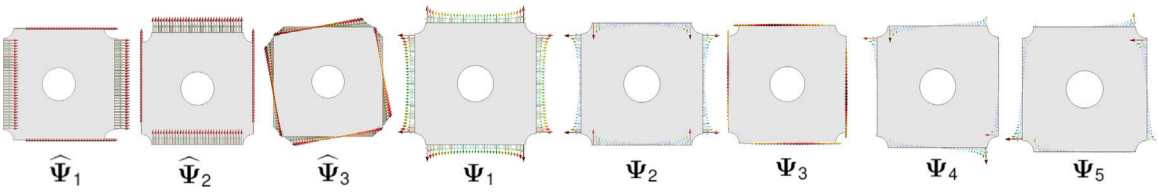

Fig. 5. Vector plot of the $n^{rb} = 3$ resultant modes $\widehat{\boldsymbol{\Psi}} = \bar{\boldsymbol{M}}\boldsymbol{R}_b$ and $p = 5$ self-equilibrated modes $\boldsymbol{\Psi}$ corresponding to the training tests displayed previously in Fig. 3. The amplitude of the self-equilibrated modes play the role of coarse-scale stresses in our formulation.

We will refer to $\widehat{\boldsymbol{\Psi}}$ as the matrix of resultant modes, since it can be readily demonstrated that the corresponding amplitudes $\boldsymbol{r} \in \mathbb{R}^{n^{rb}}$ are the resultant and moment resultants of $\boldsymbol{\lambda}$, divided by the area and moment of inertia of the interface boundary surfaces; indeed, by multiplying Eq. (8) by $\boldsymbol{R}_b^T$, and using Eq. (9), we obtain, after solving for $\boldsymbol{r}$ that $\boldsymbol{r} = \boldsymbol{G}^{-1}(\boldsymbol{R}_b^T\boldsymbol{\lambda})$, where

$$\boldsymbol{G} := \boldsymbol{R}_b^T\bar{\boldsymbol{M}}\boldsymbol{R}_b \tag{11}$$

is an $n^{rb} \times n^{rb}$ matrix containing the area and moments of inertia of the interface boundary surfaces. In Fig. 5, we show the vector plots corresponding to the $n^{rb} = 3$ resultant modes associated to the same porous domain displayed previously in Figs. 4 and 6. Moreover, although not strictly necessary, we will impose as well $\bar{\boldsymbol{M}}^{-1}$-orthogonality to the columns of $\boldsymbol{\Psi}$:

$$\boldsymbol{\Psi}^T\bar{\boldsymbol{M}}^{-1}\boldsymbol{\Psi} = \boldsymbol{I}. \tag{12}$$

We shall assume that the matrix defined by

$$\boldsymbol{H} := \boldsymbol{\Psi}^T\boldsymbol{\Phi}_b \tag{13}$$

(here $\boldsymbol{\Phi}_b = \boldsymbol{\Phi}_b(\boldsymbol{b}, :)$) is invertible. This translates in turn into the conditions

$$\texttt{ncol}(\boldsymbol{\Phi}) = \texttt{ncol}(\boldsymbol{\Psi}) = \texttt{rank}(\boldsymbol{H}). \tag{14}$$

The requirement $\texttt{ncol}(\boldsymbol{\Phi}) = \texttt{ncol}(\boldsymbol{\Psi})$ implies that, in our formulation, the number of components of the coarse-scale stress vector must be the same as the number of components of the coarse-scale strains.

If the training data only contain what we defined in Section 2.2 as basic tests, then $\boldsymbol{\Psi}$ may be computed simply by

$$[\boldsymbol{\Psi}, \boldsymbol{S}_\Psi, \boldsymbol{V}_\Psi] \leftarrow \texttt{WSVD}(\boldsymbol{K}^{\boldsymbol{\mu}}(\boldsymbol{b}, :)\boldsymbol{\Phi}, \bar{\boldsymbol{M}}^{-1}, 0), \tag{15}$$

$\boldsymbol{K}^{\boldsymbol{\mu}} \in \mathbb{R}^{N\times N}$ being the fine-scale stiffness matrix. Fig. 5 shows the vector plots of the $p = 5$ self-equilibrated modes computed this way from the deformational modes displayed previously in Fig. 4. In a more general scenario, the determination of $\boldsymbol{\Psi}$ requires first, in order to observe condition (9), the determination of the self-equilibrated component of the snapshot matrix $\boldsymbol{A}_\lambda$:

$$\widetilde{\boldsymbol{A}_\lambda} := \boldsymbol{A}_\lambda - \bar{\boldsymbol{M}}\boldsymbol{R}_b(\boldsymbol{R}_b^T\bar{\boldsymbol{M}}\boldsymbol{R}_b)^{-1}\boldsymbol{R}_b^T\boldsymbol{A}_\lambda. \tag{16}$$

In most cases, application of the weighted SVD with a truncation tolerance similar to the one used in the SVD (6) suffices to furnish self-equilibrated modes satisfying condition Eq. (14). If this is not the case, and for instance, $\texttt{ncol}(\boldsymbol{\Phi}) > \texttt{ncol}(\widehat{\boldsymbol{\Psi}})$, one should determine the subspace of $\boldsymbol{\Phi}$ that is more "aligned" to the column space of $\widehat{\boldsymbol{\Psi}}$. This can be systematically carried out by the procedure proposed by the authors for prismatic structures (but also valid here) in Ref. [15], page 12, Box 5.1.

3.3. Coarse-scale nodal displacements

Let us move now to the definition of the actual state variable of the problem: the vector of coarse-scale nodal displacements $\boldsymbol{d} \in \mathbb{R}^n$. To this end, consider a fictitious boundary mesh whose nodes coincide, in the undeformed configuration, with the nodes of the interface boundary mesh. We propose to approximate the nodal displacements of this fictitious boundary mesh, denoted by $\boldsymbol{u}^{fict} \in \mathbb{R}^M$, by the following modal expansion:

$$\boldsymbol{u}^{fict} = \boldsymbol{V}\boldsymbol{d}. \tag{17}$$

We will refer to $\boldsymbol{V} \in \mathbb{R}^{M\times n}$ as the matrix of (fictitious) interface modes. As already pointed out, interface modes are computed using standard polynomial FE shape functions. For instance, the EIFE associated to the porous domain used to illustrate the method in previous figures is a bi-unit square (canonical parent domain for quadrilaterals), and therefore, the interface modes may be readily obtained by substitution of the coordinates of the interface boundary nodes into the corresponding shape functions.

In cases where the interface boundary of a domain cannot be inscribed in a canonical parent domain, determining the interface modes $\boldsymbol{V}$ involves the construction of the inverse of the FE shape functions, since the coordinates are known in the physical domain, yet the shape functions are defined in the coordinates of the canonical parent domain. Let $\boldsymbol{x} \in \mathbb{R}^d$ denote the position of an interface boundary node, and $\boldsymbol{\xi} \in \mathbb{R}^d$ its counterpart in the parent domain. Determining the inverse mapping entails solving for $\boldsymbol{\xi}$, given $\boldsymbol{x}$, the equation $\boldsymbol{x} - \boldsymbol{X}\bar{\boldsymbol{N}}^T(\boldsymbol{\xi}) = \boldsymbol{0}$, where $\boldsymbol{X} \in \mathbb{R}^{d\times n^{nod}}$ is the matrix of nodal coordinates, and $\bar{\boldsymbol{N}} \in \mathbb{R}^{1\times n^{nod}}$ is the matrix of shape functions (assuming isoparameteric analysis). For linear shape functions, this equation is linear; for quadratic and higher orders, it may be solved via a Newton–Raphson iterative procedure (see e.g. Ref. [26]).

4. Interscale variational formulation

4.1. Stationary conditions

Following the approach advocated by the authors in Ref. [15] for the case of prismatic structures, the upscaling and downscaling relations for nodal displacement and nodal forces are determined from the stationary conditions of an energy functional of the form $\Pi = \Pi_{int} - \Pi_{ext} - \Pi_{\lambda}$, where Π_{int} stands for the internal energy, Π_{ext} denotes the contribution of external forces, while Π_{λ} is the *interface potential*. Since the employed interface modes are standard FE shape functions, the process of FE assembly, as well as the imposition of both displacement and surface tractions conditions are similar to the procedure used in standard FE implementation. For this reason, and in the interest of simplicity, we focus on just one domain with no prescribed surface tractions.

In such a case, it can be shown from the formulation presented in Ref. [15] that the stationary conditions of the energy functional Π adopts the form :

$$\delta \boldsymbol{d}^{\mu^T} \left(\boldsymbol{F}^{\mu}_{int} - \boldsymbol{F}^{\mu}_{ext} - \lambda^{all} \right) = 0, \tag{18}$$

$$\delta \lambda^T \left(\boldsymbol{d}^{\mu}_{b} - \boldsymbol{u}^{fict} \right) = 0, \tag{19}$$

$$\delta \boldsymbol{u}^{fict^T} \lambda = 0. \tag{20}$$

Here, $\delta\bullet$ symbolizes variations of its argument, $\lambda^{all} \in \mathbb{R}^N$ is a nodal vector equal to zero at every DOFs except at the interface boundary DOFs, where $\lambda^{all}(\boldsymbol{b}, :) = \lambda$, and $\boldsymbol{F}^{\mu}_{ext}$ and $\boldsymbol{F}^{\mu}_{int}$ stand for the vector fine-scale nodal external and internal forces, respectively. The variational Eqs. (18)–(20) encapsulate the equilibrium of the domain, the compatibility at the interfaces, and the equilibrium at the interfaces, respectively.

The expression for the vectors of fine-scale nodal external and internal force read

$$\boldsymbol{F}^{\mu}_{ext} := \int_{\Omega} \boldsymbol{N}^{\mu^T} \boldsymbol{f} \, d\Omega \tag{21}$$

and

$$\boldsymbol{F}^{\mu}_{int} := \int_{\Omega} \boldsymbol{B}^{\mu^T} \boldsymbol{\sigma} \, d\Omega, \tag{22}$$

respectively. In Eq. (21), $\boldsymbol{f} \in \mathbb{R}^d$ denotes body forces per unit volume (including inertial forces), whereas $\boldsymbol{B}^{\mu}$ in Eq. (22) is the standard strain–displacement "B-matrix", constructed from the gradient of $\boldsymbol{N}^{\mu}$, and relating fine-scale strains $\boldsymbol{\varepsilon} \in \mathbb{R}^s$ at a given point $\boldsymbol{x} \in \Omega$ with the fine-scale nodal displacement vector, i.e.:

$$\boldsymbol{\varepsilon}(\boldsymbol{x}) = \boldsymbol{B}^{\mu}(\boldsymbol{x}) \boldsymbol{d}^{\mu}. \tag{23}$$

By substituting modal expansions given in Eqs. (1), (8) and (17) (as well as their variations) into Eqs. (18), (19) and (20), and by exploiting the arbitrariness of $\delta\boldsymbol{\varepsilon}^c$, $\delta\boldsymbol{\sigma}^c$, $\delta\boldsymbol{a}$ and $\delta\boldsymbol{r}$, we obtain

$$\boldsymbol{\Phi}^T \boldsymbol{F}^{\mu}_{int} - \boldsymbol{\Phi}^T \boldsymbol{F}^{\mu}_{ext} - \boldsymbol{\Phi}^T_b (\bar{\boldsymbol{M}} \boldsymbol{R}_b \boldsymbol{r} + \boldsymbol{\Psi} \boldsymbol{\sigma}^c) = 0, \tag{24}$$

$$\boldsymbol{R}^T \boldsymbol{F}^{\mu}_{int} - \boldsymbol{R}^T \boldsymbol{F}^{\mu}_{ext} - \boldsymbol{R}^T_b (\bar{\boldsymbol{M}} \boldsymbol{R}_b \boldsymbol{r} + \boldsymbol{\Psi} \boldsymbol{\sigma}^c) = 0, \tag{25}$$

$$\boldsymbol{\Psi}^T (\boldsymbol{R}_b \boldsymbol{a} + \boldsymbol{\Phi}_b \boldsymbol{\varepsilon}^c) - \boldsymbol{\Psi}^T \boldsymbol{V} \boldsymbol{d} = 0, \tag{26}$$

$$\boldsymbol{R}^T_b \bar{\boldsymbol{M}} (\boldsymbol{R}_b \boldsymbol{a} + \boldsymbol{\Phi}_b \boldsymbol{\varepsilon}^c) - \boldsymbol{R}^T_b \bar{\boldsymbol{M}} \boldsymbol{V} \boldsymbol{d} = 0, \tag{27}$$

$$\delta \boldsymbol{d}^T (\boldsymbol{V}^T \bar{\boldsymbol{M}} \boldsymbol{R}_b \boldsymbol{r} + \boldsymbol{V}^T \boldsymbol{\Psi} \boldsymbol{\sigma}^c) = 0. \tag{28}$$

The preceding equations can be further simplified by, firstly, introducing orthogonality conditions (2) and (9); secondly, by using the fact that $\boldsymbol{R}^T \boldsymbol{F}^{\mu}_{int} = \boldsymbol{0}$ (nodal internal forces form a system of self-equilibrated forces); and lastly, by introducing the definition of the following matrices

$$\widehat{\boldsymbol{H}} := \boldsymbol{R}^T_b \bar{\boldsymbol{M}} \boldsymbol{\Phi}_b, \tag{29}$$

$$\boldsymbol{T} := \boldsymbol{\Psi}^T \boldsymbol{V}. \tag{30}$$

$$\widehat{\boldsymbol{T}} := \boldsymbol{R}^T_b \bar{\boldsymbol{M}} \boldsymbol{V}, \tag{31}$$

along with the definitions of $\boldsymbol{G}$ and $\boldsymbol{H}$ (given in Eqs. (11) and (13), respectively); this leads to

$$\boldsymbol{\Phi}^T \boldsymbol{F}^{\mu}_{int} - \boldsymbol{\Phi}^T \boldsymbol{F}^{\mu}_{ext} - \widehat{\boldsymbol{H}}^T \boldsymbol{r} - \boldsymbol{H}^T \boldsymbol{\sigma}^c = 0, \tag{32}$$

$$-\boldsymbol{R}^T \boldsymbol{F}^{\mu}_{ext} - \boldsymbol{G} \boldsymbol{r} = 0, \tag{33}$$

$$\boldsymbol{H} \boldsymbol{\varepsilon}^c - \boldsymbol{T} \boldsymbol{d} = 0, \tag{34}$$

$$\boldsymbol{G} \boldsymbol{a} + \widehat{\boldsymbol{H}} \boldsymbol{\varepsilon}^c - \widehat{\boldsymbol{T}} \boldsymbol{d} = 0, \tag{35}$$

$$\delta \boldsymbol{d}^T \left(\widehat{\boldsymbol{T}}^T \boldsymbol{r} + \boldsymbol{T}^T \boldsymbol{\sigma}^c \right) = 0. \tag{36}$$

4.2. Downscaling and interscale operators

The preceding system of 5 equations possesses 5 set of unknowns, namely: the coarse-scale strains ($\boldsymbol{\varepsilon}^c$), the coarse-scale stresses ($\boldsymbol{\sigma}^c$), the amplitude of the rigid-body modes ($\boldsymbol{a}$), the amplitude of the resultant modes ($\boldsymbol{r}$), and the vector of coarse-scale displacement ($\boldsymbol{d}$). The goal in the ensuing discussion is to demonstrate that, since $\boldsymbol{H}$ is assumed to be invertible, see Section 3.2, it is possible to express all the coarse-scale variables in terms of the coarse-scale nodal displacements $\boldsymbol{d}$. This will allow us, in turn, to define downscaling operators for both the deformational and rigid-components of the displacements, as well as an *intercale strain–displacement matrix*, relating fine-scale strains directly with coarse-scale nodal displacement.

Indeed, by virtue of the invertibility of $\boldsymbol{H}$, Eq. (34) can be solved for the coarse-scale strains, giving $\boldsymbol{\varepsilon}^c = \boldsymbol{H}^{-1}\boldsymbol{T}\boldsymbol{d}$. According to Eq. (1), the deformational component of $\boldsymbol{d}^\mu$ is $\check{\boldsymbol{d}}^\mu = \boldsymbol{\Phi}\boldsymbol{\varepsilon}^c$; combining this equation with the above obtained expression for the coarse-scale strains, it follows that $\check{\boldsymbol{d}}^\mu = \widetilde{\boldsymbol{U}}\boldsymbol{d}$ where

$$\widetilde{\boldsymbol{U}} := \boldsymbol{\Phi}\boldsymbol{H}^{-1}\boldsymbol{T} = \boldsymbol{\Phi}(\boldsymbol{\Psi}^T\boldsymbol{\Phi}_b)^{-1}(\boldsymbol{\Psi}^T\boldsymbol{V}) \tag{37}$$

is the *downscaling matrix for deformational displacements* —it relates the deformational component of the vector of fine-scale nodal displacements with the vector of coarse-scale nodal displacements. For later purposes, it proves convenient to cast the preceding expression as

$$\widetilde{\boldsymbol{U}} = \boldsymbol{\Phi}\widetilde{\boldsymbol{L}}\boldsymbol{V} \tag{38}$$

where

$$\widetilde{\boldsymbol{L}} := (\boldsymbol{\Psi}^T\boldsymbol{\Phi}_b)^{-1}\boldsymbol{\Psi}^T. \tag{39}$$

Inserting $\check{\boldsymbol{d}}^\mu = \widetilde{\boldsymbol{U}}\boldsymbol{d}$ into expression Eq. (23), we get

$$\boldsymbol{\varepsilon}(\boldsymbol{x}) = \boldsymbol{B}(\boldsymbol{x})\boldsymbol{d} \tag{40}$$

where

$$\boldsymbol{B}(\boldsymbol{x}) = \boldsymbol{B}^\mu(\boldsymbol{x})\widetilde{\boldsymbol{U}} = (\boldsymbol{B}^\mu(\boldsymbol{x})\boldsymbol{\Phi})\widetilde{\boldsymbol{L}}\boldsymbol{V}. \tag{41}$$

The matrix defined in the preceding equations is the aforementioned *interscale strain–displacement B-matrix*, for it connects the vector of coarse-scale nodal displacements $\boldsymbol{d} \in \mathbb{R}^n$ to the fine-scale strain vector $\boldsymbol{\varepsilon} \in \mathbb{R}^s$ at any $\boldsymbol{x} \in \Omega$.

The rigid body component of the fine-scale displacements is given, according to Eq. (1), by $\hat{\boldsymbol{d}}^\mu = \boldsymbol{R}\boldsymbol{a}$; thus, to determine the downscaling operator for rigid-body displacements ($\hat{\boldsymbol{d}}^\mu = \hat{\boldsymbol{U}}\boldsymbol{d}$), it is necessary to solve firstly Eq. (35) for $\boldsymbol{a}$; this yields $\boldsymbol{a} = \boldsymbol{G}^{-1}(\widehat{\boldsymbol{T}}\boldsymbol{d} - \widehat{\boldsymbol{H}}\boldsymbol{\varepsilon}^c)$. Then, by replacing $\boldsymbol{\varepsilon}^c$ by the expression obtained when deducing Eq. (37), and multiplying by the matrix of rigid body modes $\boldsymbol{R}$, we finally arrive at the desired expression for the *downscaling matrix for rigid body displacements*:

$$\hat{\boldsymbol{U}} := \boldsymbol{R}\boldsymbol{G}^{-1}\left(\widehat{\boldsymbol{T}} - \widehat{\boldsymbol{H}}\boldsymbol{H}^{-1}\boldsymbol{T}\right) = \boldsymbol{R}\,\hat{\boldsymbol{L}}\,\boldsymbol{V}, \tag{42}$$

where

$$\hat{\boldsymbol{L}} := (\boldsymbol{R}_b^T\bar{\boldsymbol{M}}\boldsymbol{R}_b)^{-1}\boldsymbol{R}_b^T\bar{\boldsymbol{M}}\left(\boldsymbol{I} - \boldsymbol{\Phi}_b(\boldsymbol{\Psi}^T\boldsymbol{\Phi}_b)^{-1}\boldsymbol{\Psi}^T\right) \tag{43}$$

Lastly, since $\hat{\boldsymbol{d}}^\mu = \hat{\boldsymbol{U}}\boldsymbol{d}$ and $\check{\boldsymbol{d}}^\mu = \widetilde{\boldsymbol{U}}\boldsymbol{d}$, it follows from Eq. (1) that

$$\boldsymbol{d}^\mu = (\hat{\boldsymbol{U}} + \widetilde{\boldsymbol{U}})\boldsymbol{d} = \boldsymbol{U}\boldsymbol{d} \tag{44}$$

where

$$\boldsymbol{U} = \hat{\boldsymbol{U}} + \widetilde{\boldsymbol{U}} \tag{45}$$

is the downscaling matrix for nodal displacements.

4.3. Coarse-scale nodal forces

We next draw our attention to Eq. (36). This variational equation encapsulates the condition of coarse-scale equilibrium equation—it involves coarse-scale stresses and the coarse-scale resultants of the external forces. We seek to cast this equation in terms of the fine-scale vectors of nodal internal forces ($\boldsymbol{F}^\mu_{int}$) and external forces ($\boldsymbol{F}^\mu_{ext}$). To this end, we solve first Eq. (33) for $\boldsymbol{r}$:

$$\boldsymbol{r} = -(\boldsymbol{R}\boldsymbol{G}^{-1})^T\boldsymbol{F}^\mu_{ext}. \tag{46}$$

Then we plug the above equation into Eq. (32), and solve it for the coarse-scale stress vector $\boldsymbol{\sigma}^c$; this furnishes, after some rearrangements:

$$\boldsymbol{\sigma}^c = (\boldsymbol{\Phi}\boldsymbol{H}^{-1})^T\boldsymbol{F}^\mu_{int} - \left(\boldsymbol{\Phi}\boldsymbol{H}^{-1} - \boldsymbol{R}\boldsymbol{G}^{-1}\widehat{\boldsymbol{H}}\boldsymbol{H}^{-1}\right)^T\boldsymbol{F}^\mu_{ext}. \tag{47}$$

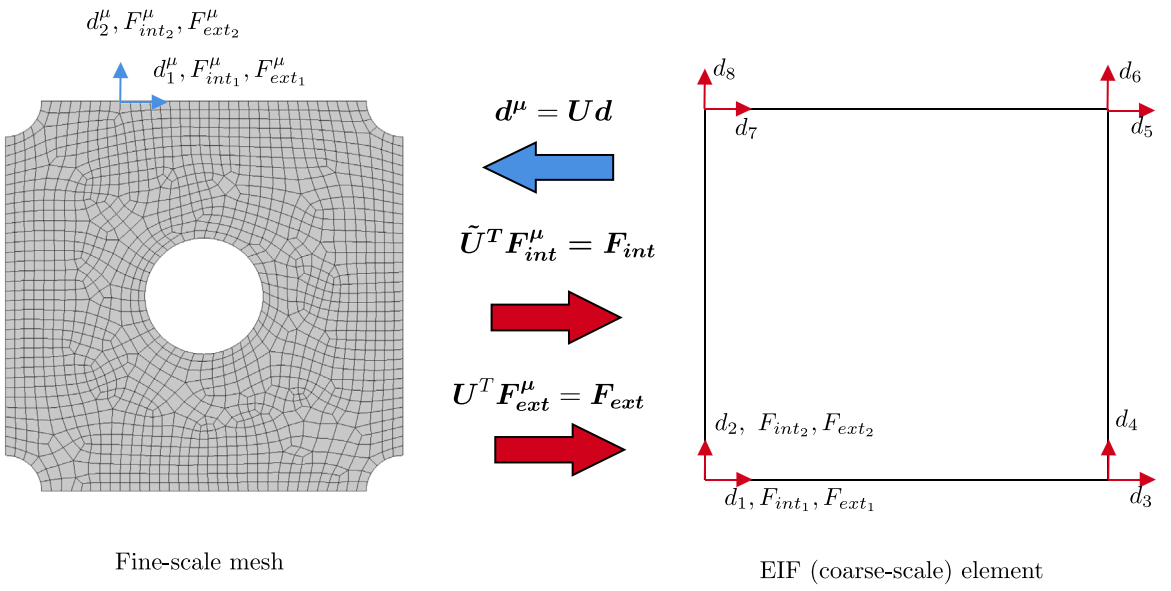

Fig. 6. Left: Schematic representation of fine-scale variables, namely, nodal displacements ($\boldsymbol{d}^\mu$), internal forces ($\boldsymbol{F}_{int}^\mu$) and external forces ($\boldsymbol{F}_{ext}^\mu$), in a porous domain discretized with 1384 Q9 elements ($N = 11460$ DOFs). Right: Coarse-scale counterparts ($\boldsymbol{d}, \boldsymbol{F}_{int}, \boldsymbol{F}_{ext}$) in the corresponding coarse-scale linear EIFE ($n = 8$ DOFs).

Finally, substitution of the preceding two equations into the variational equilibrium equation (36), and gathering the terms multiplying both $\boldsymbol{F}_{int}^\mu$ and $\boldsymbol{F}_{ext}^\mu$, we find, upon carefully inspection, that the matrices multiplying $\boldsymbol{F}_{int}^\mu$ and $\boldsymbol{F}_{ext}^\mu$ are but the transposes of the downscaling matrices $\tilde{\boldsymbol{U}}$ and $\boldsymbol{U}$, respectively, i.e.:

$$\delta \boldsymbol{d}^T \left(\tilde{\boldsymbol{U}}^T \boldsymbol{F}_{int}^\mu - \boldsymbol{U}^T \boldsymbol{F}_{ext}^\mu \right) = \boldsymbol{0}. \tag{48}$$

The above equation suggests to define the vectors of coarse-scale nodal internal forces and nodal external forces by

$$\boldsymbol{F}_{int} := \tilde{\boldsymbol{U}}^T \boldsymbol{F}_{int}^\mu \tag{49}$$

and

$$\boldsymbol{F}_{ext} := \boldsymbol{U}^T \boldsymbol{F}_{ext}^\mu, \tag{50}$$

respectively. Note that, in doing so, $\tilde{\boldsymbol{U}}^T$ and $\boldsymbol{U}^T$ adopt the role of *upscaling matrices* for nodal internal and nodal external forces, respectively.

For clarity, these various upscaling/downscaling relationships deduced so far are illustrated in Fig. 6.

4.4. Final interscale formulation (parent domain)

By combining the expressions for the fine-scale internal forces in Eq. (22), and the interscale strain–displacement matrix in Eq. (41), we can rewrite the coarse-scale internal forces in Eq. (51) as

$$\boldsymbol{F}_{int} = \int_\Omega \boldsymbol{B}^T \boldsymbol{\sigma}\ d\Omega. \tag{51}$$

Likewise, for the coarse-scale (tangent) stiffness matrix, using Eq. (40), we have

$$\boldsymbol{K} := \frac{\partial \boldsymbol{F}_{int}}{\partial \boldsymbol{d}} = \int_\Omega \boldsymbol{B}^T \frac{\partial \boldsymbol{\sigma}}{\partial \boldsymbol{\epsilon}} \frac{\partial \boldsymbol{\epsilon}}{\partial \boldsymbol{d}}\ d\Omega = \int_\Omega \boldsymbol{B}^T \boldsymbol{C} \boldsymbol{B}\ d\Omega. \tag{52}$$

where $\boldsymbol{C} := \partial \boldsymbol{\sigma} / \partial \boldsymbol{\epsilon}$ denotes the constitutive tangent matrix.

Remark 4.1. The above expressions reveal that, as opposed to other reduced-order multiscale methods based on computational homogenization [5–7], in the proposed formulation, the coarse-scale internal forces and tangent stiffness matrix are directly linked to the Cauchy stresses $\boldsymbol{\sigma}$ and the corresponding constitutive tangent matrix $\boldsymbol{C}$ at the fine-scale (without the need of solving a nested sequence of local/global problems). In fact, the reader familiar with basic FE theory will immediately recognize that expressions (51) and (52) are formally identical to those of the elemental internal force vector and stiffness matrix of a standard FE formulations (see e.g. Ref. [27])—the adopted notational scheme is precisely intended to highlight this very fact. The only difference is the definition

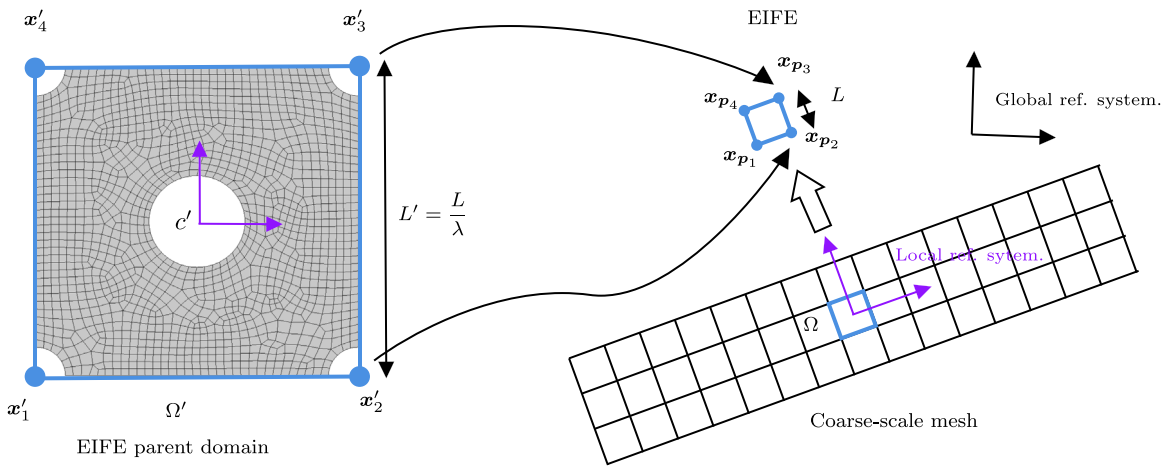

Fig. 7. Concepts of EIFE parent domain and EIF element. The rigid body, deformational and self-equilibrated modes ($\boldsymbol{R}$, $\boldsymbol{\Phi}$ and $\boldsymbol{\Psi}$, respectively) are expressed in the local reference system of the parent domain. The mapping between points of the parent domain Ω' and physical domain Ω is given by Eq. (56).

of the strain–displacement matrix $\boldsymbol{B}$, which in this case, as reflected in Eq. (41), is not simply the gradient of a polynomial shape functions, but rather depends on basis matrices $\boldsymbol{\Psi}$ and $\boldsymbol{\Phi}$ derived from the training data.

Remark 4.2. The stability of the proposed method hinges crucially on the spectral properties of the previously defined element stiffness matrix $\boldsymbol{K}$, in particular, in its positive definiteness. In Appendix A we postulate the conditions that the self-equilibrated modes have to observed in order for the method to be stable.

The same logic employed to deduce Eq. (51) can be applied to arrive at the interscale expression for the vector of external body forces. Indeed, if we define the interscale counterpart of the shape function matrix $\boldsymbol{N}^{\mu}$ by

$$\boldsymbol{N}(\boldsymbol{x}) := \boldsymbol{N}^{\mu}(\boldsymbol{x})\boldsymbol{U}. \tag{53}$$

and then combine this equation with Eq. (50) and Eq. (21), we obtain

$$\boldsymbol{F}_{ext} := \int_{\Omega} \boldsymbol{N}^T \boldsymbol{f}\, d\Omega. \tag{54}$$

Likewise, since $\boldsymbol{f}$ include inertial forces, we may write the *coarse-scale mass matrix* as

$$\boldsymbol{M}_{\rho} := \int_{\Omega} \boldsymbol{N}^T \rho \boldsymbol{N}\, d\Omega. \tag{55}$$

4.5. Final interscale formulation (arbitrary size and orientation)

In deriving the interscale operators defined in the foregoing, it was assumed that the EIF element in the coarse-scale mesh has the same size and orientation as the trained domain. A more general scenario is depicted in Fig. 7, wherein the physical domain $\Omega \subset \mathbb{R}^d$ associated to a given EIF element is related to the trained or EIFE parent domain $\Omega' \subset \mathbb{R}^d$ by a combination of translation, rotation and uniform scaling, i.e.:

$$\boldsymbol{x} = \boldsymbol{t} + \lambda \boldsymbol{Q}(\boldsymbol{x}' - \boldsymbol{c}'). \tag{56}$$

Here, $\boldsymbol{x} \in \Omega$, $\boldsymbol{x}' \in \Omega'$, $\boldsymbol{c}'$ denotes the centroid of the parent domain, $\boldsymbol{t} \in \mathbb{R}^d$ stands for the translation vector, $\lambda \in \mathbb{R}$ designates the scaling factor, and $\boldsymbol{Q} \in \mathbb{R}^{d\times d}$ is the rotation matrix ($\boldsymbol{Q}^T\boldsymbol{Q} = \boldsymbol{I}$). In Appendix B, we outline a procedure for determining $\boldsymbol{t}$, $\boldsymbol{Q}$ and λ from the nodal coordinates of the EIF element.

The rotation matrix appearing in Eq. (56) relates nodal displacement vectors expressed in the local reference system (see Fig. 7) with their counterparts in the global reference system, at both scales, i.e.: $\boldsymbol{d}^{\mu}_J = \boldsymbol{Q}\boldsymbol{d}^{\mu'}_J$ and $\boldsymbol{d}_j = \boldsymbol{Q}\boldsymbol{d}'_j$ (here primed variables represent local coordinates, and J and j refer to fine-scale and coarse-scale nodes, respectively). These transformations can be compactly written for all the nodes of both the domain mesh and the interface boundary mesh by

$$\boldsymbol{d}^{\mu} = \boldsymbol{Q}_N \boldsymbol{d}^{\mu'}, \qquad \boldsymbol{d} = \boldsymbol{Q}_n \boldsymbol{d}' \tag{57}$$

where $\boldsymbol{Q}_N$ and $\boldsymbol{Q}_n$ denote $N \times N$ and $n \times n$ block diagonal matrices, respectively, containing repetitions of $\boldsymbol{Q}$ (i.e., $\boldsymbol{Q} = \text{diag}\,(\boldsymbol{Q}, \boldsymbol{Q}, \ldots \boldsymbol{Q})$). The preceding equations allow us, upon simple matrix manipulations, to deduce the expressions in global coordinates of the downscaling matrices defined previously, in local coordinates, in Eqs. (42) and (38); these expressions read:

$$\widetilde{\boldsymbol{U}} = (\boldsymbol{Q}_N\boldsymbol{\Phi})\widetilde{\boldsymbol{L}}(\boldsymbol{V}\boldsymbol{Q}_n^T), \tag{58}$$

$$\widehat{\boldsymbol{U}} = (\boldsymbol{Q}_N \boldsymbol{R})\widehat{\boldsymbol{L}}(\boldsymbol{V}\boldsymbol{Q}_n^T). \tag{59}$$

Likewise, the interscale matrix $\boldsymbol{N}$ in the physical domain can be simply obtained as

$$\boldsymbol{N} = \boldsymbol{Q}\boldsymbol{N}'\boldsymbol{Q}_n^T \tag{60}$$

$\boldsymbol{N}'$ being the matrix defined in Eq. (53) for the EIFE parent domain; this follows easily from the fact that the fine-scale shape function $\boldsymbol{N}^{\mu}$ in Eq. (53) is invariant to deformations of the domain.

By contrast, the interscale strain–displacement matrix $\boldsymbol{B}$ is defined in terms of the gradient of the shape functions in the EIFE parent domain $\boldsymbol{B}^{\mu}$ (see Eq. (53)), which is not invariant under rotations nor scaling; thus, deriving its expression in the actual physical configuration requires the computation of the gradient matrix in such a configuration. This can be done by rotating each of the columns of $\boldsymbol{B}^{\mu}$ (which represents unit virtual strains), and dividing the resulting matrix by the scaling factor λ. Alternatively, one may skip this step by working with strains and stress expressed in the local reference system. In doing so, the interscale strain–displacement becomes expressible as

$$\boldsymbol{B} = 1/\lambda \boldsymbol{B}'\boldsymbol{Q}_n^T, \tag{61}$$

$\boldsymbol{B}'$ being the matrix defined.[1] in Eq. (41). This approach may prove advantageous when dealing with curved elements, in which stresses and strains are more naturally represented in the local reference system of the subdomain rather than in global coordinates.

5. Numerical approximation of element vectors and matrices (hyperreduction)

Let us address now the problem of how to numerically approximate the integrals appearing in the definition of the element vectors of internal and external body forces (Eqs. (51) and (54), respectively). The goal is to devise *cubature* rules of the form

$$\boldsymbol{F}_{\boldsymbol{int}} = \int_{\Omega} \boldsymbol{B}^T \boldsymbol{\sigma}\, d\Omega \approx \lambda^d \sum_{g=1}^{m^{int}} w_g^{int} \boldsymbol{B}(\boldsymbol{x}_g^{int})^T \boldsymbol{\sigma}(\boldsymbol{x}_g^{int}), \tag{62}$$

$$\boldsymbol{F}_{\boldsymbol{ext}} := \int_{\Omega} \boldsymbol{N}^T \boldsymbol{f}\, d\Omega \approx \lambda^d \sum_{g=1}^{m^{ext}} w_g^{ext} \boldsymbol{N}(\boldsymbol{x}_g^{ext})^T \boldsymbol{f}(\boldsymbol{x}_g^{ext}). \tag{63}$$

In Eq. (62), $\boldsymbol{x}_g^{int} \in \Omega$ and $w_g^{int} > 0$ denote the position and weight, respectively, of the gth integration point ($g = 1, 2 \dots m^{int}$); the same variables for the external (body) forces in Eq. (63) are denoted by $\boldsymbol{x}_g^{ext} \in \Omega$ and by $w_g^{ext} > 0$ ($g = 1, 2 \dots m^{ext}$). The scaling factor λ^d ($d = 2, 3$) is introduced to account for the change of size of the physical domain Ω with respect to the EIFE parent domain Ω' (this factor is the Jacobian of the transformation introduced in Eq. (56)). It follows from Eq. (52) and Eq. (55) than, in adopting the above cubature rules, the element tangent stiffness matrix $\boldsymbol{K}$ and the element mass matrix $\boldsymbol{M}_{\rho}$ are approximated by

$$\boldsymbol{K} \approx \lambda^d \sum_{g=1}^{m^{int}} w_g^{int} \boldsymbol{B}(\boldsymbol{x}_g^{int})^T \boldsymbol{C}(\boldsymbol{x}_g^{int}) \boldsymbol{B}(\boldsymbol{x}_g^{int}), \tag{64}$$

$$\boldsymbol{M}_{\rho} \approx \lambda^d \sum_{g=1}^{m^{ext}} w_g^{ext} \boldsymbol{N}(\boldsymbol{x}_g^{ext})^T \rho(\boldsymbol{x}_g^{ext}) \boldsymbol{N}(\boldsymbol{x}_g^{ext}). \tag{65}$$

The requirement of positive weights ($w_g^{int} > 0$) in the internal force rule is introduced to ensure that, if $\boldsymbol{C}$ is positive definite, then $\boldsymbol{K}$ is semipositive definite (positive definite if rigid body displacements are constrained; note that this is further predicated upon the satisfaction of the stability criterion (70)). A similar reasoning can be put forward for the case of the weights w_g^{ext} employed in the calculation of the mass matrix.

5.1. Continuous empirical Cubature method

To derive such cubature rules, we use the Continuous Empirical Cubature Method (CECM) [8], advocated by the first author and collaborators in Ref. [8] for general hyperreduction problems, and briefly described in what follows. We focus on the cubature rule for the internal forces in Eq. (62)—the guidelines given for this case can be readily extended to the case of body forces in Eq. (63).

Let $\boldsymbol{X}^{\mu} = \{\boldsymbol{x}_1^{\mu}, \boldsymbol{x}_2^{\mu} \dots \boldsymbol{x}_G^{\mu}\}$ denote the positions of the Gauss points of the underlying (fine-scale) finite element mesh, and $\boldsymbol{W}^{\mu} = [W_1^{\mu}, W_2^{\mu}, \dots W_G^{\mu}]$ the corresponding vector of (positive) weights. The first step in the CECM is to build a matrix $\boldsymbol{D}^{\mu}$ (that we will call the integrand matrix) containing the values of the internal work per unit volume at all Gauss points $\boldsymbol{X}^{\mu}$ and for all the training scenarios considered in the problem. If only basic training tests are used, it can be readily shown that the integrand matrix may be computed simply as

$$\boldsymbol{D}^{\mu}(k, i\, j) = \boldsymbol{B}_i(\boldsymbol{x}_k^{\mu})^T \boldsymbol{C}(\boldsymbol{x}_k^{\mu}) \boldsymbol{B}_j(\boldsymbol{x}_k^{\mu}), \qquad k = 1, 2 \dots G, \qquad i, j = 1, 2 \dots n, \tag{66}$$

[1] For economy of notation, we have introduced a minor notational inconsistency, for the matrix derived in Eq. (41) for the reference domain is denoted by the same bare symbol as the matrix in the right-hand side of Eq. (61) (which is for the physical domain). The same applies to Eq. (60) and Eq. (53)

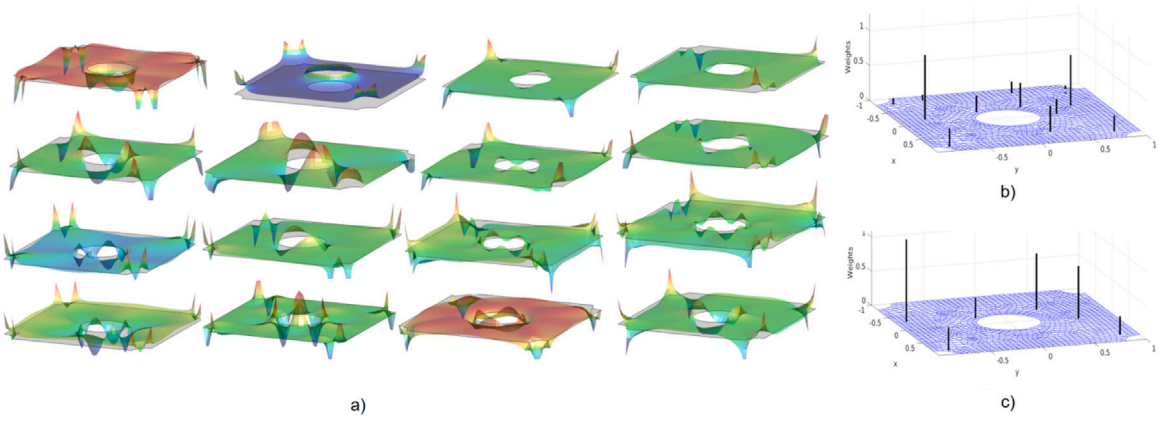

Fig. 8. (a) Surface plots of the $q = 16$ integrand basis functions corresponding to the linear basic training of the porous domain displayed previously in Figs. 4 and 5. (b) Location of the $q = 16$ integration points and corresponding weights of a Cubature rule produced in the first step of the solution of the sparsification problem (68). (c) Final cubature rule with $m^{int} = 6$ points obtained in the second sparsification step by using as initial guess the points and weights shown in plots 8.b. The underlying FE mesh (also shown in the plots) has $G = 1384 \cdot 9 = 12456$ Gauss points.

(the size of $\boldsymbol{D}^{\mu}$ in this case is $G \times n^2$). The next step in the CECM is to determine an (approximated) $\boldsymbol{W}^{\mu}$-orthogonal basis matrix for the column space of the integrand matrix $\boldsymbol{D}^{\mu}$, computed using the weighted SVD as follows:

$$[\boldsymbol{J}^{\mu}, \bullet, \bullet] \leftarrow \texttt{WSVD}(\boldsymbol{D}^{\mu}, \text{diag}\,(\boldsymbol{W}^{\mu}), \epsilon_{int}), \tag{67}$$

The columns of matrix $\boldsymbol{J}^{\mu}$ are the discrete representations of L_2-orthogonal basis functions for the integrand. A continuous representation of these functions, referred to hereafter by $\boldsymbol{J} = \boldsymbol{J}(\boldsymbol{X})$, can be computed by fitting a polynomial function to the values of $\boldsymbol{J}^{\mu}$ on each element of the fine-scale mesh (so that $\boldsymbol{J}(\boldsymbol{X}^{\mu}) = \boldsymbol{J}^{\mu}$). In addition, since the CECM requires the volume of the domain be exactly integrated, $\boldsymbol{J}^{\mu}$ is to be augmented with a column accounting for this constraint. For instance, for the case of the linear EIF element ($n = 8$) of the porous domain shown in previous figures, this process returns 16 orthogonal functions[2]; by way of illustration, the surface plots of these 16 functions are displayed in Fig. 8.a.

After computing the matrix $\boldsymbol{J}^{\mu}$, the CECM seeks a cubature rule for *exactly* integrating the basis functions represented by the columns of $\boldsymbol{J}^{\mu}$, using as few points as possible, while ensuring that the weights are positive. If the weights solution $\boldsymbol{W}$ is regarded as a vector of the same size as $\boldsymbol{W}^{\mu}$, then the condition "as few points as possible" translates into the problem of minimizing the number of non-zero components of $\boldsymbol{W}$. Accordingly, the cubature problem can be posed as that of finding a weight vector $\boldsymbol{W} \in \mathbb{R}^G$ and the corresponding positions $\boldsymbol{X} = \{\boldsymbol{x}_1, \boldsymbol{x}_2, \ldots \boldsymbol{x}_G\}$ such that

$$\begin{aligned} \min_{\boldsymbol{W},\boldsymbol{X}} \quad & \|\boldsymbol{W}\|_0 \\ \text{s.t.} \quad & \boldsymbol{J}(\boldsymbol{X})^T \boldsymbol{W} = \boldsymbol{c} \\ & \boldsymbol{W} \geq \boldsymbol{0} \\ & \boldsymbol{X} \subset \Omega. \end{aligned} \tag{68}$$

Here, $\boldsymbol{c} = \boldsymbol{J}^{\mu^T} \boldsymbol{W}^{\mu}$ is the vector of "exact" integrals; $\|\boldsymbol{W}\|_0$ denotes the so-called ℓ_0 *pseudo-norm* of $\boldsymbol{W}$ – this pseudo-norm counts the number of non-zero entries of a vector, see e.g. [28] –; and the notation $\boldsymbol{W} \geq \boldsymbol{0}$ means that all components of $\boldsymbol{W}$ are non-negative.

Ref. [8] proposes to solve the preceding sparsification problem in two steps. In the first step, the positions of the points are held fixed ($\boldsymbol{X} = \boldsymbol{X}^{\mu}$), and the method determines a non-negative, sparse solution of the underdetermined system of equations $\boldsymbol{J}^{\mu^T} \boldsymbol{W}^{\mu} = \boldsymbol{c}$. We use for this purpose the greedy algorithm developed by the first author in Appendix A of Ref. [10] —referred to hereafter as the Discrete Empirical Cubature Method (DECM). Since the system is underdetermined, the solution is not unique. In the employed DECM, one can elicit different solutions by changing the initial set of candidate points. We show in Fig. 8.b one possible cubature rule corresponding to a particular set of candidate points for the integration of the $q = 16$ functions displayed previously in Fig. 8.a.

In the second step of the CECM, the sparsification problem (68) is addressed considering both positions and weights as design variables, and taking as initial guess the one obtained in the previous step. The sparsification algorithm proceeds by zeroing one weight at a time (usually the point with smallest non-zero weight), and readjusting the positions and weights of the remaining points so that the constraints of the problem are satisfied. In Fig. 8.c, we show the 6-points cubature rule produced in this step using as initial guess the rule shown in Fig. 8.b.

[2] The initial set contains $8^2 = 64$ integrand functions. However, there are only 5 deformational modes, and besides $\boldsymbol{C}$ is symmetric; this means that only $(5 + 1)5/2 = 15$ functions are linearly independent.

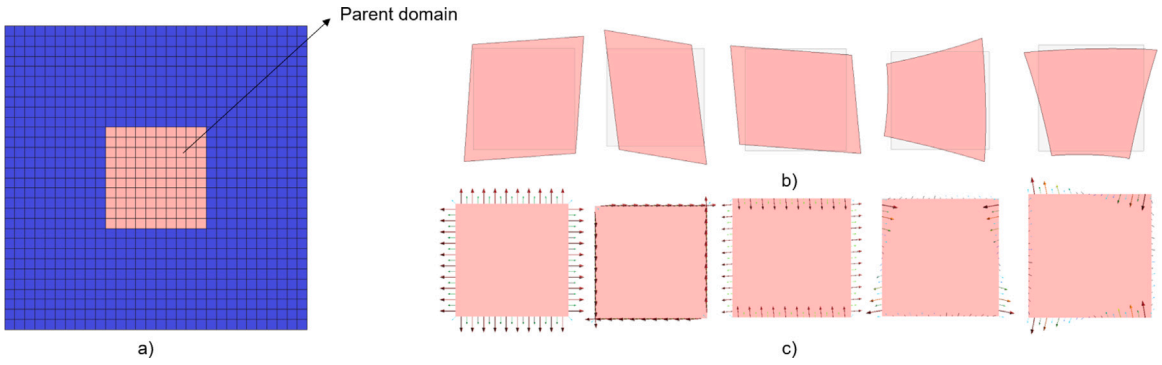

Fig. 9. (a) Domain used to train the EIFE parent domain for the case of near-incompressible elastic material (Poisson's ratio $\nu = 0.499$). (b) $p = 5$ deformational modes obtained from the $n = 8$ training tests. (c) Corresponding self-equilibrated modes.

The recipe for computing the cubature rule for body forces (63) is essentially the same as the one described in the foregoing for the internal forces, the only difference being the definition of the integrand matrix, which depends on the type of body forces acting on the domain. If only inertial forces are considered, this matrix can be calculated as

$$\bar{\boldsymbol{D}}^{\mu}(k,i\,j) = \boldsymbol{N}_i(\boldsymbol{x}_k^{\mu})^T \rho(\boldsymbol{x}_k^{\mu}) \boldsymbol{N}_j(\boldsymbol{x}_k^{\mu}), \qquad k = 1,2\ldots G, \qquad i,j = 1,2\ldots n. \tag{69}$$

6. Numerical assessment

6.1. Nearly-incompressible homogeneous material

We begin the validation of the proposed Empirical Interscale FEM by examining the performance of the method in dealing with structures made of homogeneous materials. To this end, we choose the limiting case of nearly-incompressible isotropic elastic material, characterized by a Young's Modulus $E = 70$ GPa, and Poisson's ratio $\nu = 0.499$ (in plane strain). Quadrilateral linear elements (4 nodes per element) will be used for the EIFE method, and will be compared with the standard (irreducible) FE method, using both linear quadrilateral (Q4) and quadratic quadrilateral elements (Q9). We consider the case in which all coarse-scale elements are square, and therefore, only one parent domain is to be trained.

6.1.1. Offline operations

We take as EIFE parent domain a bi-unit square with a structured fine-scale mesh of 10×10 quadratic quadrilaterals (Q9), featuring $N = 441 \cdot 2 = 882$ fine-scale DOFs and $G = 100 \cdot 9 = 900$ fine-scale Gauss points. The training domain is formed by 3×3 cells, the EIFE parent domain being the one in the middle (see Fig. 9.a), and only the $n = 8$ basic training tests are carried out. Fig. 9.b and 9.c show the $p = n - n^{rb} = 5$ deformational and self-equilibrated modes, respectively obtained in such tests.

As for the cubature rule for internal forces per unit volume, Fig. 10.a shows the $q = 6$ basis functions obtained from the weighted SVD, out of the $n^2 = 64$ functions given by Eq. (66) (using a threshold $\epsilon_{int} = 10^{-3}$ for the SVD). The second step of the CECM finally manages to reduce the number of points from $q = 6$ to $m^{int} = 3$. The corresponding cubature rule is displayed in Fig. 10.b. In the other cubature rule, for inertial forces (mass matrix), the number of basis functions for the integrand function turns out to be $\bar{q} = 17$ (using the same tolerance as in the case of internal forces), and the second sparsification step leads finally to a final rule of $m^{ext} = 7$ points.

6.1.2. Static deformation

Two problems will be employed to assess the accuracy of the obtained EIF element, namely: the static deformation of a 2D fixed-fixed beam (plane strain) subjected to a uniformly distributed load on its top surface; and the determination of the natural frequencies of such a structure. The sketch of the first problem is displayed in Fig. 11.a, wherein we show the 3 types of elements used in the assessment: the EIFE Q4 (4 nodes) with 3 CECM integration points, the FE Q4 with 4 Gauss points, and the FE Q9 (9 nodes) with 9 Gauss points. Figs. 11.b, 11.c and 11.d display the deformed shapes of the domain (discretized into 4×80 elements) along with the contour plot of Von Mises stresses computed using these 3 types of elements. In Fig. 11.b, the fine-scale stresses for the EIFE case are determined in a (post-processing) reconstruction stage by first computing the strains at all the Gauss points of the fine-scale mesh via Eq. (40), and then evaluating the stresses produced by such strains by the corresponding elasticity matrix.

The qualitative resemblance between the stress distributions and deformed shapes of Figs. 11.b (EIFE Q4) and 11.d (FE Q9) is notable. The only perceptible difference is that the stress distribution is slightly less smooth in the EIFE Q4 case than in the FE Q9—this is to be expected, because the degree of continuity demanded by the EIFE method is lower than in the case of the standard FE method. This fact can be further corroborated in the magnified view of Fig. 11.b, where the scaling factor has been set to 20 in order to reveal the noticeable jump in displacement occurring between the fine-scale domains of contiguous coarse-scale elements. Despite this lack of fine-scale continuity, in quantitative terms, the agreement with respect to the FE Q9 solutions is notorious: the

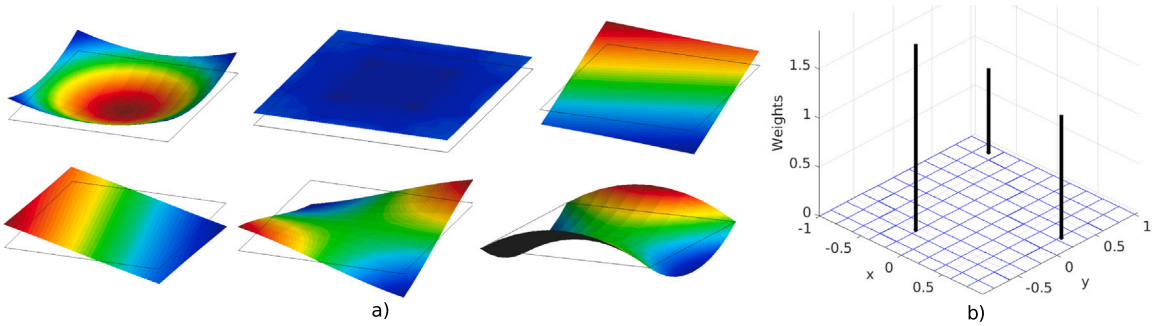

Fig. 10. Parent domain made of homogeneous, near-incompressible material (Poisson's ratio $\nu = 0.499$). (a) Surface plots of the $q = 6$ basis functions for the internal forces per unit volume. (c) Location and weights of the $m^{int} = 3$ points determined by the Continuous Empirical Cubature Method (CECM) by solving the sparsification problem (68).

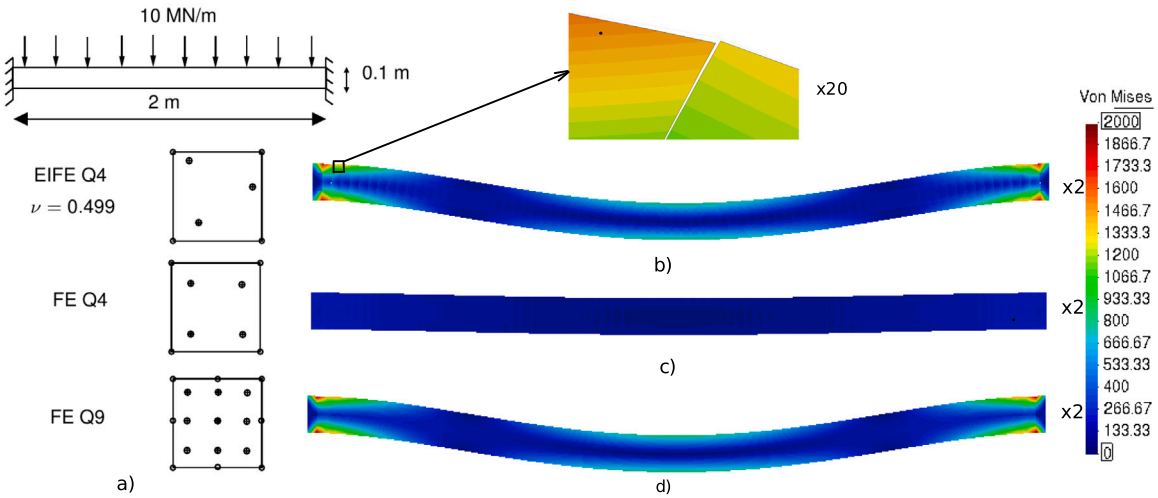

Fig. 11. (a) Boundary conditions for the prismatic structure (plane strain, made of homogeneous elastic material with Poisson's ratio $\nu = 0.499$) used to assess the accuracy of the proposed formulation, along with the 3 types of elements employed in the assessment. The EIFE Q4 has 4 nodes and 3 integration points (obtained via the CECM, see Fig. 10.b). The strain–displacement matrix $\boldsymbol{B}$ at these 3 points are computed by Eq. (61). The other two elements, FE Q4 and FE Q9, are the standard linear and quadratic elements, featuring 4 and 9 nodes/integration points, respectively. (b) Contour plot of the (fine-scale) Von Mises stresses obtained with the EIFE Q4 element. Deformed shape is amplified by a factor of 2. The enlarged view has an amplification factor of 20, so as to appreciate the discontinuity between coarse-scale elements (c) and (d) Von Mises stresses and deformed shapes computed by the FE Q4 and FE Q9, respectively.

EIFE Q4 predicts a maximum displacements of 5.44 cm, while the FE Q9 yields 5.41 cm (i.e., the EIFE Q4 is 0.55% more flexible than the FE Q9); as for the strain energy, the EIFE Q4 gives[3] 0.290 MJ, and the FE Q9 0.288 MJ (0.69% of discrepancy).

This level of accuracy of the proposed EIFE Q4 element with respect to the FE Q9 element is in stark contrast to its FE counterpart, the standard Q4 element which, as can be appreciated in Fig. 11.c, grossly underpredicts both stresses and displacements (it gives a maximum displacement of 0.76 cm, 86% lower than the prediction of our EIFE Q4). This lack of accuracy is due to the well-studied phenomenon of volumetric locking (consult e.g. Ref. [29], Chapter 8), present in low-order elements. Our EIFE Q4 element does not suffer from this undesirable phenomenon because the deformational modes are not compatible with the Q4 linear kinematics (this can be observed by examining the rightmost modes of Fig. 9.b, which exhibits curved boundaries typical of bending deformations).

6.1.3. Convergence upon mesh refinement

Further quantitative insight can be gained from the mesh refinement analysis depicted in Fig. 12, which contains the results of 6 different analyses varying the number of elements through thickness (1, 2, 4, 8, 16 and 32). The analyzed variable is the difference of strain energy with respect to the finer mesh (32 × 640) using Q9 elements, which predicts a strain energy of $E_{ref} = 0.2949$ MJ. Fig. 12.a compares the performance of the two Q4 elements, and Fig. 12.b displays the comparison of the EIFE Q4 and the FE Q9 elements. The former graph highlights again the wide disparity between the predictive capabilities of our EIFE Q4 elements with respect to the standard Q4 elements. The other graph reveals an interesting fact: the level of accuracy of the EIFE Q4 elements is

[3] Strain energy in the EIFE is calculated using just the 3 integration points of each element.

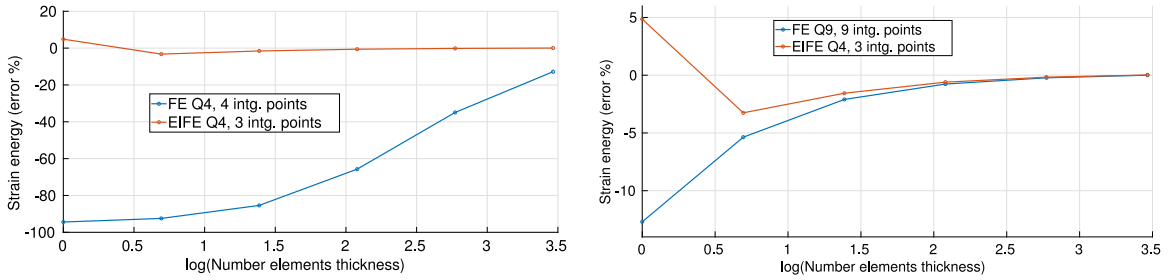

Fig. 12. Mesh refinement analysis for the problem depicted in Fig. 11.a, for meshes of 1, 2, 4, 8, 16 and 32 elements through the thickness (square elements). Case of nearly-incompressible homogeneous material ($\nu = 0.499$). The analyzed variable is the difference of strain energy with respect to the finest mesh (32×640) using Q9 elements. (a) FE Q4 and EIFE Q4 elements. (b) EIFE Q4 and FE Q9 elements.

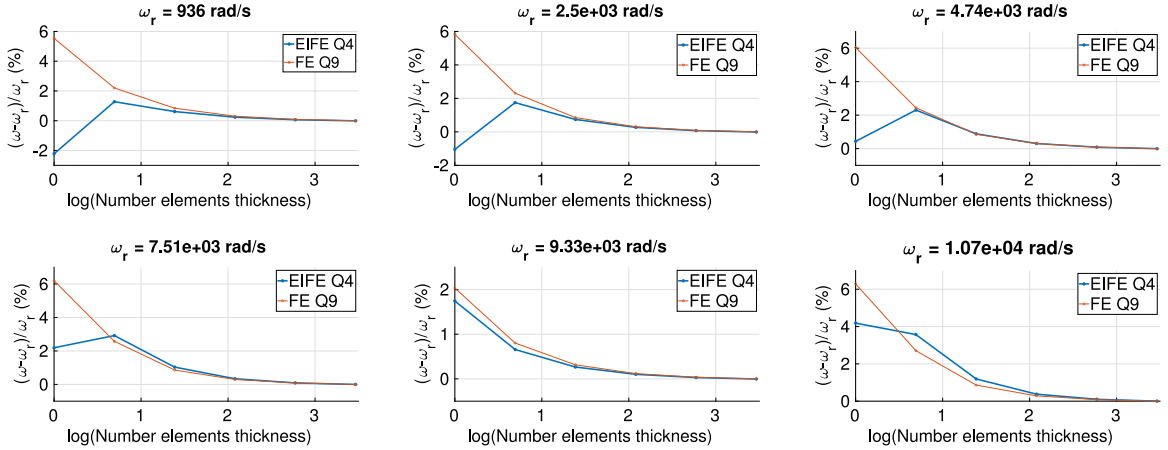

Fig. 13. Mesh refinement analysis in terms of the first 6 natural frequencies of the fixed-fixed beam depicted in Fig. 11.a. Case of nearly-incompressible homogeneous material ($\nu = 0.499$). Each graphs show the difference between the predictions obtained for each mesh with respect to the reference value, which is that furnished by the finest mesh using FE Q9 elements.

higher than the Q9 elements for all levels of discretization—despite the fact that it employs approximately half the number of DOFs, and three times less integration points.

6.1.4. Natural frequencies

The assessment presented in the foregoing discussion provides convincing proof of the accuracy of the *trained* EIFE Q4 element in representing static bending deformations for nearly-incompressible material—and, in doing so, it substantiates the correctness of the proposed interscale scheme in terms of the strain–displacement matrix $\boldsymbol{B}$ (see Eq. (61)) and the cubature rule for internal forces (displayed in Fig. 10), which are the ingredients appearing in the approximation of the coarse-scale stiffness matrix in Eq. (64). In the following, we carry out the assessment a step further and examine the consistency of the approximations involved in the definition of the coarse-scale mass matrix in Eq. (65) (density equal to $\rho = 2.7 \cdot 10^{-3}$ Kg/m^3).

To this end, we conduct a mesh refinement analysis similar to the one shown in Fig. 12, but in terms of the natural frequencies of the fixed-fixed beam of Fig. 11.a. Results are displayed in Fig. 13. Inspection of the six graphs indicates that the predictions of the EIFE Q4 element converges to the reference solution for the six frequencies, the maximum discrepancy being at all cases below 4%. For the first three frequencies, the EIFE Q4 results are more accurate than their FE Q9 counterparts; for the other frequencies, this trend is progressively reversed, yet the level of accuracy are still quite similar.

In conclusion, the results obtained in this mesh refinement analysis demonstrates that the EIFE Q4 yields accuracy levels comparable to those furnished by the FE Q9 element. These findings reinforce the consistency and validity of the underlying interscale scheme, as they confirm the correctness of the upscaling scheme for inertial forces (encoded in expression (53)).

6.2. Heterogeneous material

We continue the validation of the method by assessing its performance in modeling heterogeneous periodic structures. The unit cell selected for this study is the porous domain used in preceding sections to illustrate various aspects of the method. The dimensions of the parent domain of this element, as well as its underlying fine-scale mesh, are shown in Fig. 14.a and 14.b, respectively.

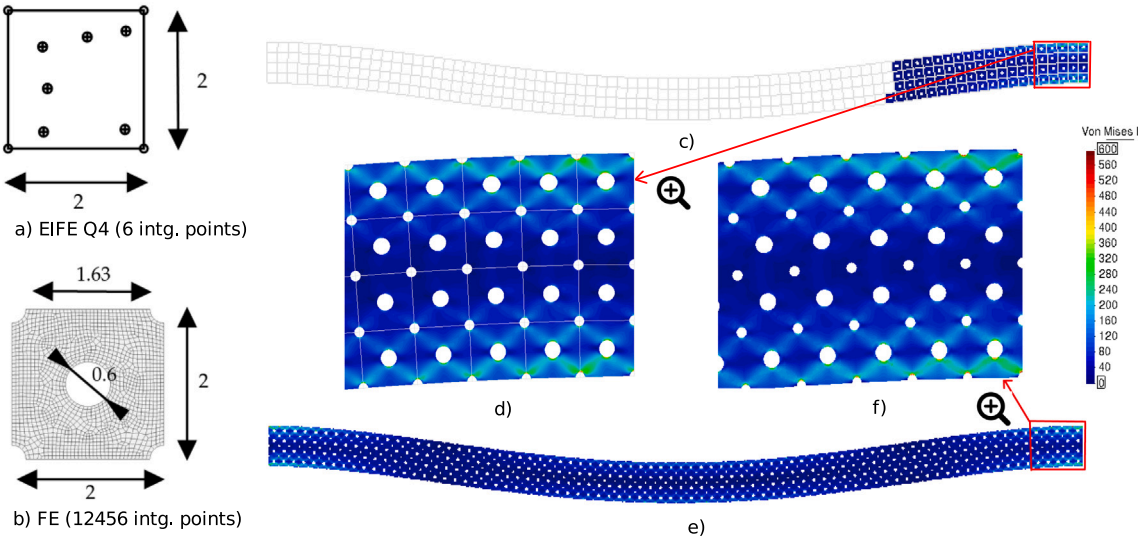

Fig. 14. Static deflection of a fixed-fixed beam (plane strain) made of porous material. (a) Parent domain of the coarse-scale EIF element used in the analysis, featuring 4 corner nodes, and 6 integration points determined by the CECM (see Fig. 8.c). (b) Dimensions of the porous unit cell corresponding to the EIF element, along with its (fine-scale) mesh. (c) Deformed shape (×10) of the coarse-scale model of the beam, consisting of 4 × 80 EIF elements. The deformed shapes of the unit cells and contour plots of fine-scale Von Mises stresses (in MPa) associated to the rightmost elements are also displayed. Some of these reconstructed cells are shown in magnified view in Fig. 14.d. (e) Deformed shape (×10) and contour plot of Von Mises stresses corresponding to the Direct Numerical Simulation (DNS). (f) Enlarged view of the rightmost cells of this DNS analysis. (For interpretation of the references to color in this figure legend, the reader is referred to the web version of this article.)

6.2.1. *Offline stage*

The fine-scale mesh consists of 1384 Q9 elements (this gives a total of $G = 1384 \cdot 9 = 12456$ Gauss points), and $N = 11460$ DOFs. The employed 3×3 training domain was shown previously in Fig. 2.a. The material is assumed to behave linearly elastically during the training tests, with Young's Modulus $E = 70000$ MPa, and Poisson's ratio $\nu = 0.3$.

We first focus on deriving a coarse-scale element with 4 nodes (EIFE Q4). As mentioned in Section 3.1, the $n = 8$ basic training tests (sketched previously in Fig. 2) give rise to the $p = 5$ deformational and self-equilibrated modes depicted in Figs. 4 and 5. On the other hand, we take as cubature rule for internal forces the one shown in Fig. 8.c (featuring $m^{int} = 6$ points). A similar procedure for inertial forces lead to a 12-points points for such forces. Thus, our EIF element features $n = 8$ DOFs, $m^{int} = 6$ integration points for internal forces, and $m^{ext} = 12$ points for body forces. In dimensionality reduction terms, this implies a reduction in number of DOFs of $N/n = 1432.5$, and a reduction of integration points of $G/m^{int} = 2076$ for internal forces, and $G/m^{ext} = 1038$ for body forces.

6.2.2. *Static deformation of a fixed-fixed beam (elastic range)*

The predicting capabilities of this coarse-scale EIF element are examined in the same problem employed in the previous section, namely, the static deformation of the fixed-fixed beam produced by an uniformly distributed load on its top surface (the dimensions of the beam are the same as those shown in Fig. 11). The beam is formed by 4×80 repeated copies of the porous unit cell under study. The uniformly distributed load in this case is equal to $P_{fe} = 1.227$ MPa.

Fig. 14.e shows the deformed shape and the contour plot of Von Mises stresses corresponding to the so-called Direct Numerical Simulation (DNS), that is, the solution of this problem using the standard FE without any simplifying assumption. To keep the comparison as fair as possible, the discretization used for each of the 320 subdomains is the same as the fine-scale mesh of the parent domain in Fig. 14.b, thus resulting in a FE mesh with a total of $12456 \cdot 320 \approx 4$ millions Gauss points. The maximum displacement predicted by this DNS model is 9.1 mm, and the strain energy is 4.91 KJ. An enlarged view of the right end of the beam is shown in Fig. 14.f.

On the other hand, the deformed shape of the coarse-scale model of the beam, featuring 4×80 EIFE Q4 elements, is displayed in Fig. 14.c. Since this EIF element employs the same integration rules for evaluating boundary traction integrals than the standard FE method, the applied load in this case is to be scaled by $\alpha = 1.63/2$ (see Fig. 14.b), giving a distributed load of $P_{eife} = \alpha P = 1.0$ MPa.

This coarse-scale model predicts a maximum displacement of 8.96 mm, and a strain energy of 4.80 KJ. The deviations with respect to the DNS results are therefore 1.54% for displacements and 2.26% for strain energy. Thus, despite the fact that the coarse-scale model requires over 1000 times less DOFs and integration points with respect to the DNS, the loss of accuracy is below 2.5%. This is specially remarkable in the computation of the strain energy: the 4.91 KJ furnished by the DNS are calculated as a weighted sum of the product of strains and stresses at the 4 millions Gauss points of the mesh, while the prediction of 4.80 KJ of the EIFE model only employs $6 \times 320 = 1920$ integration points (and the difference is only 2.26%). This fact provides compelling evidence that the interscale strain–displacement matrix $\boldsymbol{B}(\boldsymbol{x})$ in Eq. (61) at the $m^{int} = 6$ integrations points and weights computed by the CECM effectively encode all the necessary fine-scale features relevant for obtaining reasonably accurate predictions at the coarse scale.

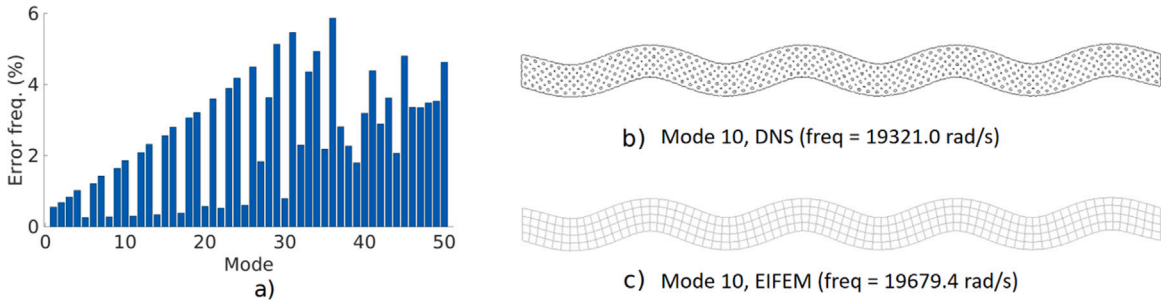

Fig. 15. (a) Difference (in %) between the natural frequencies predicted by the EIFEM and the DNS, in the case of the fixed-fixed beam formed by 4 × 80 cells. (b) and (c) Deformed shapes of the 10th mode computing by both the DNS and the EIFEM, respectively.

The proposed EIF element offers the user the possibility of recovering, in a post-process stage, on demand, any fine-scale variable. For instance, in Fig. 14.c, we reconstruct the displacements and Von Mises stresses of 77 of the 320 subdomains. The magnifed view of Fig. 14.d allows one to qualitatively compare the quality of the predictions with respect to the DNS (shown in Fig. 14.f). Except for the cells in contact to the surface with constrained displacements, in which the reconstructed stresses are slighly less intense than the ones in the DNS model, the remaining regions exhibit similar stress patterns—the discrepancies at the Dirichlet boundary are to be expected because, after all, the EIF element has not been "taught" in the training stage to capture such local effects. Nevertheless, despite these minor discrepancies, the coarse-scale model is still able to detect the stress peaks at the pores.

6.2.3. Natural frequencies and modes

We complete the assessment of the fixed-fixed beam problem in the linear elastic range by comparing the natural frequencies and natural modes provided by the DNS and the coarse-scale model (again for a configuration of 4 × 80 cells). Density is equal to $\rho = 2.7 \cdot 10^{-3}$ Kg/m^3). In Fig. 15.a, we show the difference between the natural frequencies obtained by the EIFEM and the DNS (with respect to the former frequencies, in %) for the first 50 modes. The error is below 1% for the first 5 modes; then it increases linearly for some of the modes (a more detailed analysis, not shown here, reveals that these are bending-dominated modes), up to a maximum of 5,8%; then it seems to become stable around 3.5 %. The average error for these 50 modes is 2.5%, a figure that can be deemed satisfactory for engineering purposes—specially considering that the number of DOFs in the eigenvalue problem for the coarse-model is 1000 times smaller than the one for the DNS. By way of illustration, we show in Figs. 15.b and 15.c the deformed shapes of the 10th mode provided by both models (in this case, the EIFEM frequency is 1.85% higher).

6.2.4. Mesh convergence analysis

Since we have conferred the "status" of finite element to our coarse-scale representation of the unit cell, it is natural to wonder to which solution would converge the method if we progressively increase the resolution of the mesh (if it converges at all). Intuitively, as the size of the EIF element becomes smaller, so does the unit cell associated to this element, and therefore, one may argue that it should converge to the solution obtained in the limiting scenario of *scale separation*. This solution is provided by first-order homogenization (see e.g. Ref. [30]), which, in the elastic range, boils down to carry out a standard FE analysis in which the structure is assumed to be continuous, and in which (coarse-scale) stresses are evaluated using the *homogenized elasticity matrix* of the unit cell.

To corroborate whether this intuitive reasoning is correct, we conduct in the following a mesh refinement analysis for the problem of the fixed-fixed beam subjected to uniformly distributed load. We use discretizations with 2, 4, 8, 16 and 32 elements through the thickness of the beam. To determine the homogenized elasticity matrix of the porous unit cell, we first extrude the unit cell in the perpendicular direction to the plane – so as to create a 3D unit cell –, and then run 4 FE analyses using *periodic boundary conditions*. In each of these analyses, the interface boundary of the cell is deformed according to strain states in which one entry is set to 1, and the remaining entries to 0, as illustrated in Fig. 16. The homogenized elasticity matrix $\boldsymbol{C}^{hom}$ is formed by arranging in columns the volumetric average stresses (in-plane normal stresses, in-plane shear stress, and out-of-plane normal stress) determined from these tests; we also show in Fig. 16 this matrix.

The strain energy predicted by the homogenized FE method with the finest mesh (32 × 640) and Q9 elements is 4.82 KJ. We take this value as the reference solution and measure the deviations of the EIFE Q4 predictions with respect to this value. The plot of this error (in %) versus the logarithm of the number of thickness elements is displayed in Fig. 17. For completeness, we also show in this Figure the graph obtained by FE homogenization using standard Q4 elements. Inspection of the two graphs shown in Fig. 17 reveals that, not only does the *EIFE Q4 solution converge to the reference, homogenized solution* (as conjectured), but the deviations at all levels of resolution are significantly lower than those of the homogenized FE Q4 element. For instance, for the case of two elements through the thickness (mesh 2 × 40), the discrepancy between the EIFE prediction and the reference solution is only 0.46%, while the homogenized FE Q4 model incurs in an error of 13.37%.

The fact that our EIFE Q4 element gives values closer to the "exact" homogenized solution than the standard FE Q4 element equipped with a homogenized constitutive equation might seem paradoxical at first, because the latter element assumes that scale

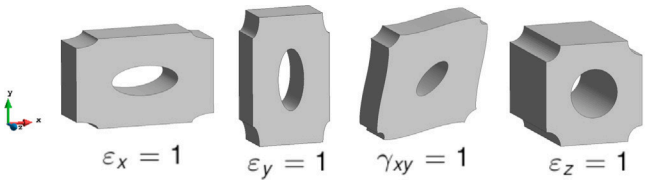

$$\boldsymbol{C}^{hom} = E \begin{bmatrix} 0.99 & 0.412 & 0 & 0.42 \\ 0.412 & 0.99 & 0 & 0.42 \\ 0 & 0 & 0.301 & 0 \\ 0.42 & 0.42 & 0 & 1.16 \end{bmatrix}$$

Fig. 16. Computation of the homogenized elasticity matrix ($\boldsymbol{C}^{hom}$) for the porous unit cell. The displayed deformed shapes corresponds to 4 FE analyses with periodic boundary conditions. In each of these tests, the interface boundary is deformed according to strain states in which one entry is set to 1, and the remaining entries to zero. The homogenized elasticity matrix $\boldsymbol{C}^{hom}$ is formed by arranging in columns the average stresses determined from these tests.

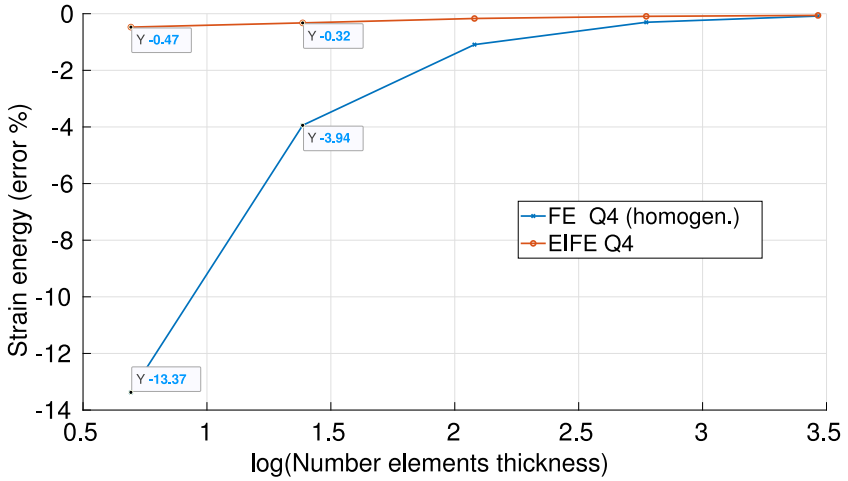

Fig. 17. Mesh refinement analysis for the problem of the fixed-fixed beam made of porous material and subjected to a uniformly distributed load on its top surface (plane strain). The coarse-scale meshes have 2, 4, 8, 16 and 32 elements through the thickness (square elements). The analyzed variable is the difference of strain energy for each of these discretizations with respect to the finest mesh (32 × 640) using Q9 elements, and in which strains and stresses at each of the Gauss points of the element is established via the homogenized elasticity matrix displayed in Fig. 16. The FE Q4 graph corresponds to the predictions of the standard Q4 elements using this very homogenized elasticity matrix. The other graph corresponds to values obtained when using the EIFE Q4 element sketched in Fig. 14.a—recall that this is an interscale element and, thus, the relation between stresses and strains at its integration points (in this case 6 points) is established using the elasticity matrix of the constituent material (not the homogenized one).

separation holds regardless of the size of the finite element, while the EIF element does not presuppose scale separation at all. The higher error observed in the case of the standard FE Q4 elements is to be attributed to the tendency of these elements to experience volumetric locking in bending problems; as demonstrated in Section 6.1, our EIFE Q4 elements does not suffer from this drawback, hence the higher accuracy.

6.2.5. *Static deformation of a fixed-fixed beam (elastoplastic range)*

According to the preceding study, the proposed EIF element can be legitimately used in place of homogenized elements for analyzing problems in which the scale separation hypothesis holds. Furthermore, using the proposed EIFE method has the advantage over homogenization methods that, in the EIFE method, one can reconstruct the displacement and stress fields of several contiguous cells and thus form a clear picture of what are the deformation mechanisms at the fine-scale (see for instance Fig. 14); in FE homogenization, by contrast, this can be only done at Gauss point level, by post-processing individual unit cells, and therefore, such overall picture cannot be obtained.

Yet the truly distinct advantage of the EIFE method with respect to computational homogenization emerges when dealing with (material) *nonlinear analyses*. Indeed, in computational homogenization, nonlinear material analyses require the deployment of a complex algorithmic infrastructure in which, each time the coarse-scale stresses is to be computed at a Gauss point, it is necessary to solve a boundary value problem using as input parameter the coarse-scale strain at such a point, either by the FE method itself (this is the so-called FE^2 approach [3]), or by any reduced-order variants of such a method [4–7]. This is because the integration points in computational homogenization are points of an *homogenized continuous medium* whose actual constitutive behavior is unknown. By contrast, in the proposed EIFE method, the integration points are not points of any homogenized continuous medium, but pertains to the underlying fine-scale structure—this is why we call the method “interscale” in the first place. Accordingly, switching from linear elastic constitutive equations to more general, nonlinear constitutive equations requires no more effort than changing the constitutive laws associated to each of the integration points of the element.

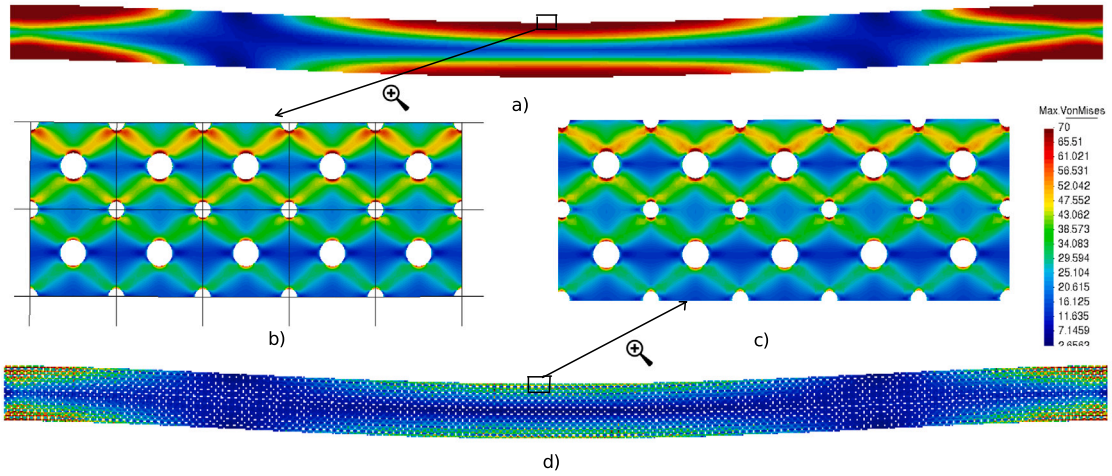

Fig. 18. Fixed-fixed beam made of porous material subjected to a uniformly distributed load on its top surface (plane strain). Imposed load is 0.35 MPa. The material obeys a Von Mises (J2) elastoplastic model (linear isotropic hardening law), with yield stress $\sigma_y = 70$ MPa, and hardening modulus $H = 10^{-6}E$. (a) Deformed shape (×10) and smoothed contour plot of Von Mises maximum stresses at each one of the 8×320 EIF elements. (b) Reconstruction of the Von Mises stresses at 8 of the cells located at the mid-span. (c) and (d) Contour plot of Von Mises stresses provided by the DNS.

To illustrate this point, we have taken the same problem studied in the foregoing in the linear elastic range (fixed-fixed beam with prescribed load on its top surface), and simply change the constitutive model to a Von Mises (J2) elastoplastic model, endowed with linear isotropic hardening law, with yield stress $\sigma_y = 70$ MPa, and negligible hardening modulus ($H = 10^{-6}E$).

Examining how localization of strains due to plastic yielding propagates throughout the structure and finally produce the collapse of the structure would require first training the unit cell in such extreme scenarios, and then determining the corresponding deformational and interface force modes. Selecting which trajectories to use in the training is a challenging task in its own right, due to the sheer number of possible combinations, and it is out of the scope of the present work. Rather, we adopt a more pragmatic approach and use the same basic training tests employed for the elastic range, and therefore, the same deformational and interface modes obtained in such tests. To improve the accuracy, we limit ourselves to increase the number of integration points, from the 6-points rule used previously, to the 16-points rule determined in the first stage of the CECM selection procedure (see Fig. 8.b) —it may be argued that integration points act as strain and stress "sensors", in the sense that the model will only see what happens at these very points; therefore, the higher the number of points, the higher the accuracy.

Fig. 18 compares the results obtained with the EIFE model and the DNS, for the case of 8×320 unit cells. The imposed load is 0.35 MPa for the EIFE model, and $0.35 \cdot (2/1.63) = 0.43$ MPa for the DNS, using 35 time steps for both cases. The constitutive differential equations are integrated in time using the classical, fully implicit backward-Euler scheme (see e.g. [31]). Fig. 18.d displays the deformed shape (×10) and contour plot of Von Mises stresses for the DNS, with an enlarged view in Fig. 18.c of the 8 cells located at mid-span, wherein it can be appreciated that plastic yielding has already initiated at the regions around the pores (the Von Mises stress is equal to the yield stress at these regions), and start to spread along straight paths formed between adjacent pores. Fig. 18.a, on the other hand, shows the coarse-scale representation of the Von Mises stresses calculated by the EIFEM. The displayed contour plot corresponds to the (smoothed) distribution of maximum Von Mises stress at the integration points of each EIF element. This representation allows us to readily identify all the regions in which plastic yielding has started. As pointed out earlier, a more detailed analysis can be carried out by reconstructing, in the post-process stage, the stresses at any desired location. For instance, in Fig. 18.c, we show the stresses in the same region shown for the DNS in Fig. 18.d. The qualitative and quantitative resemblance between the DNS predictions and the stresses provided by the EIFE is notorious. It should be pointed out that the stresses at the shown cells are determined by integrating in time the J2 constitutive equations at all the Gauss points of the selected cells, using as source term the fine-scale strains obtained by multiplying the downscaling matrix $\widetilde{\boldsymbol{U}}$ times the history of coarse-scale displacements.

In terms of computational savings, the DNS features more than 1 million Q9 elements, while the EIFE model only has 2560 Q4 elements. The 35 steps of the DNS took approximately 1 h in an in-house, vectorized FE MATLAB code operating in a Linux platform[4]; the time required for the EIFE analysis (using exactly the same FE code, but with different element technology) is about 10 s (including the post-process reconstructions)—so the computational speedup is about 360. This speedup factor is calculated without taking into account the offline cost of running the FE training analyses and constructing the bases, since such computations have to be performed just once. In the case at hand, the FE training process required around 18 s.

[4] Intel(R) Core(TM) i7-8700, with 12 processors at 3.20 GHz (RAM 64 Gbytes)

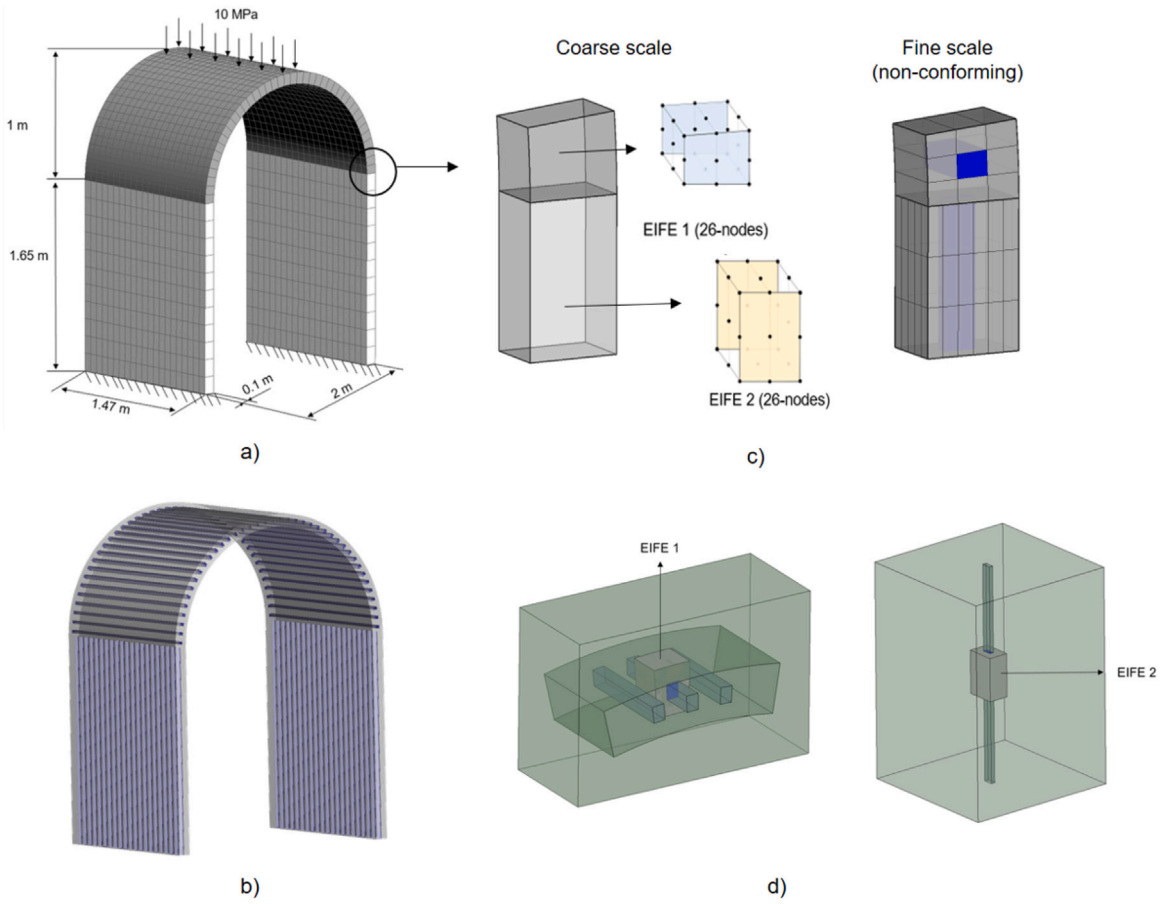

Fig. 19. (a) Coarse-scale discretization for the structure being analyzed, with corresponding size and boundary conditions. (b) Heterogeneous pillar-supported tunnel. (c) EIF element types and corresponding non-conforming subgrids (materials illustrated in different colors—blue for the fibre and gray for the matrix). (d) Domains used to train the EIFE parent elements.

6.3. Multiple three-dimensional heterogeneous parent domains

We conclude the numerical evaluation of the proposed method by demonstrating its ability to deal with multiple heterogeneous three-dimensional EIFE parent domains with non-matching subgrids. To this end, the pillar-supported tunnel depicted in Fig. 19.b will be evaluated under a uniformly distributed force using quadratic hexahedral EIF elements and compared against results given by the standard FEM. Fig. 19.c shows the two fibre-reinforced subdomains, namely the arch (EIFE type 1) and the pillar domain (EIFE type 2), and their corresponding non-conforming subgrids. EIFE type 1 is discretized into 9 tri-quadratic (27 nodes) hexahedra elements, featuring $N = 147 \cdot 3 = 441$ fine-scale DOFs and $G = 9 \cdot 27 = 243$ Gauss points, while EIFE type 2 contains 90 tri-quadratic hexahedrons, featuring $N = 1001 \cdot 3 = 3003$ fine-scale DOFs and $G = 90 \cdot 27 = 2430$ fine-scale Gauss points. Both domains contain a matrix characterized by an isotropic elastic material with a Young's Modulus $E = 70000$ MPa and a Poisson's ratio of $\nu = 0.3$. The fibre, on the other hand, is characterized by another isotropic elastic material 10 times stiffer than the matrix ($E = 700000$ MPa, $\nu = 0.3$).

Fig. 19.d shows the training structures for the arch and pillar elements, which contain the corresponding EIFE parent domains in the middle, and also, matrix/fibre surrounding materials. As detailed in Section 2, the selection of the training boundary conditions depends on the choice made regarding the nodes (or shape functions) that describe the frame of the parent domain. In this case, as a result of using tri-quadratic hexahedra elements, there are 27 nodes describing the element, but 26 of them are located in the frame (the remaining node is an interior node). Thus, a total of $n = 26 \cdot 3 = 78$ basic training tests were conducted, resulting in $p = n - n^{rb} = 72$ deformational modes for each EIFE parent domain. With regards to the cubature rule for internal forces per unit volume, using a threshold of $\epsilon_{int} = 10^{-3}$, the CECM computed a total of $m^{int} = 72$ and $m^{int} = 102$ integration points for the EIFE 1 and EIFE 2 parent domains, respectively.

The problem sketched in Fig. 19.a is proposed to be solved by both DNS and the EIFEM. The standard FEM requires the construction of a conforming fine grid (117180 tri-quadratic hexahedrons in this case), while our method requires conformity only at the coarse-scale level, leading to a discretization of 1302 EIF elements. Note that, in terms of DOFs, we are reducing from more

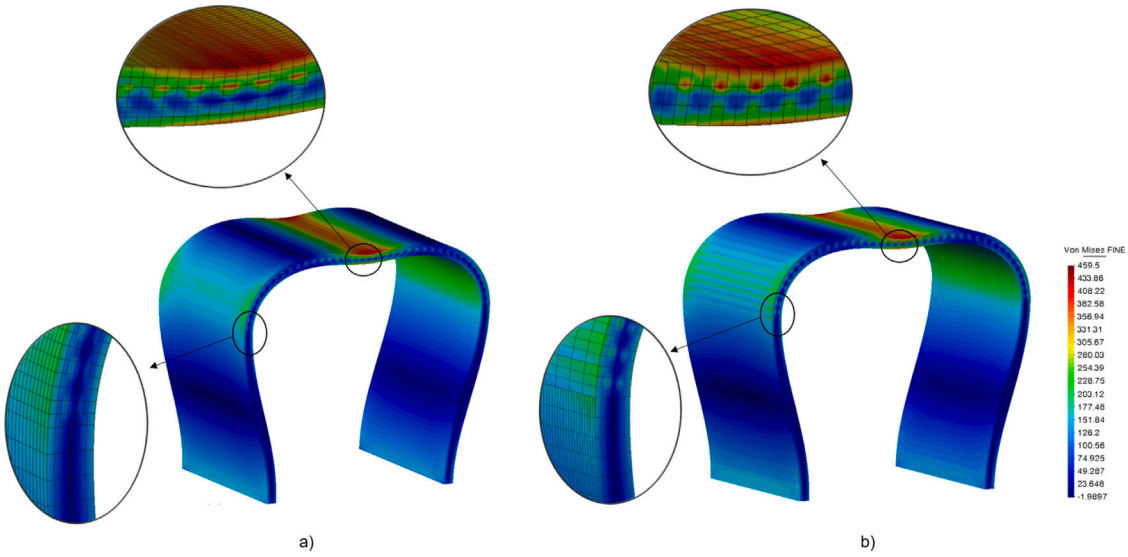

Fig. 20. Contour plot of the (fine-scale) Von Mises stresses on the deformed shape of the tunnel structure (amplified by a factor of 1.5). (a) Solution computed by the standard FEM. (b) Reconstructed (fine-scale) solution obtained by the EIFEM. Enlarged views to highlight the agreement on the solution, despite discontinuity of stresses between coarse-scale elements for the EIFEM.

than 3 million DOFs in the standard method to 44469 DOFs for the EIFEM, giving a reduction factor of almost 70. Figs. 20.a and 20.b display the deformed shapes of the tunnel domain (amplified by a factor of 1.5) along with the contour plot of Von Mises stresses obtained by both methods. Note that, on the EIFEM, fine-scale stresses are determined in a post-processing stage after the computation of the coarse-scale solution. As shown in Fig. 20, despite the remarkable reduction of DOFs for the EIFEM, the resemblance to the FEM solution is noticeable. The only difference that can be observed is that the EIFEM solution exhibits jumps between coarse-scale elements, resulting in a slight lack of smoothness. However, Von Mises stresses are still very similar for both methods. In terms of displacements, the EIFEM predicts a maximum value of 0.2544 m, while the DNS yields 0.2543 m. The agreement of the solution is again striking, obtaining a EIF element with just 0.01% more flexibility than the standard FE.

7. Concluding remarks

This paper has presented a novel approach to multiscale finite element analysis for heterogeneous media. Traditional finite element implementations assume homogeneity and continuity within the elements, requiring homogenization procedures for non-homogeneous cases. However, the proposed method demonstrates that by adjusting the number and location of integration points, the corresponding weights, and the definition of strain–displacement matrices, the original constitutive laws of the constituents can be preserved without the need for complex nested solvers or analytical approximations.

The approach presented here is not entirely new, as the idea of modifying integration points and B-matrices to enhance finite element properties has been previously explored—for instance, the idea underlying the “B-bar” formulations for avoiding locking phenomena is quite similar (see e.g. Ref. [32], pag. 181). However, the distinguishing feature of the proposed method is that the expressions for the B-matrices, as well as the integration point locations and weights, are derived automatically from full-order finite element tests, rather than being proposed by FE theorists using analytical approximations. This systematic procedure, which rests on a solid variational formulation, allows for the automatic mining of these FE data and opens up new possibilities for creating extensive finite element libraries for modeling heterogeneous media.

The paper acknowledges that further research is required to address the training of the method in the inelastic range, as well as the inclusion of bubble modes to widen its scope. Additionally, extending the formulation to handle large deformations with moderate strains is another direction for future exploration. It is expected that as the system enters fully in the inelastic range, the number of modes and the complexity of the problem will increase significantly, potentially requiring nonlinear parameterizations and reduced-order modeling techniques such as local SVD bases, polynomial manifolds, or autoencoders. These approaches have shown promise in the general literature on reduced-order modeling (consult e.g. [33,34] for local bases, [35,36] for polynomial manifolds, and [37] for autoencoders) and can provide benefits in terms of low-parametrization and improved hyperreduction.

Last but not least, the interscale nature of the proposed method offers opportunities for studying multiple scales concurrently. Starting from the bottom scale, substructures can be trained and integration points determined. This process can be repeated at each higher scale until reaching the coarsest scale where engineering predictions are needed. This way the nodal internal forces at this “engineering” scale may be linked directly to the stresses at the bottom of the scale hierarchy. Ongoing investigations are exploring these avenues and will be reported in forthcoming publications.

Declaration of competing interest

The authors declare that they have no known competing financial interests or personal relationships that could have appeared to influence the work reported in this paper.

Data availability

Data will be made available on request.

Acknowledgments

This work has received support from the Spanish Ministry of Economy and Competitiveness, through the "Severo Ochoa Programme for Centres of Excellence in R&D" (CEX2018-000797-S)". The authors acknowledge the support of "MCIN/AEI/10.13039/501100011033/y por FEDER una manera de hacer Europa" (PID2021-122518OB-I00). A. Giuliodori also gratefully acknowledges the support of "Secretaria d'Universitats i Recerca de la Generalitat de Catalunya i del Fons Social Europeu" through the FI grant (00939/2020), and J.A. Hernández the support of, on the one hand, the European High-Performance Computing Joint Undertaking (JU) under grant agreement No. 955558 (the JU receives, in turn, support from the European Union's Horizon 2020 research and innovation programme and Spain, Germany, France, Italy, Poland, Switzerland, Norway), and the European Union's Horizon 2020 research and innovation programme under Grant Agreement No. 952966 (project FIBREGY).

Appendix A. Stability considerations

A.1. Stability condition

In this appendix, we address the issue of the stability of the resulting system of EIFE equations, based on the expression for the coarse-scale tangent stiffness matrix in Eq. (70). As we demonstrate in what follows, matrix $\boldsymbol{T} \in \mathbb{R}^{p\times n}$ defined in Eq. (30) —which represents the work done by the p self-equilibrated force modes $\boldsymbol{\Psi}$ over the n interface displacement modes $\boldsymbol{V}$, must meet the following condition

$$\texttt{rank}(\boldsymbol{T}) = n - n^{rb} \tag{70}$$

(recall that $n^{rb} = 3$ or 6 are the number of rigid-body modes).

The demonstration consists in showing that Eq. (70) ensures that if the constitutive tangent matrix $\partial\boldsymbol{\sigma}/\partial\boldsymbol{\varepsilon}^c$ in Eq. (52) is positive definite, then, the *constrained* element stiffness matrix inherits this desirable attribute. We begin by writing the element stiffness matrix $\boldsymbol{K} \in \mathbb{R}^{n\times n}$ defined in Eq. (52) in terms of its fine-scale counterpart $\boldsymbol{K}^{\boldsymbol{\mu}} \in \mathbb{R}^{N\times N}$:

$$\boldsymbol{K} = \widetilde{\boldsymbol{U}}^T \boldsymbol{K}^{\boldsymbol{\mu}} \widetilde{\boldsymbol{U}} = (\boldsymbol{\Psi}^T \boldsymbol{V})^T \boldsymbol{H}^{-T} (\boldsymbol{\Phi}^T \boldsymbol{K}^{\boldsymbol{\mu}} \boldsymbol{\Phi}) \boldsymbol{H}^{-1} (\boldsymbol{\Psi}^T \boldsymbol{V}) \tag{71}$$

where we have used the expression for the downscaling matrix $\widetilde{\boldsymbol{U}}$ in Eq. (37). By *constrained* element stiffness matrix we mean the stiffness matrix resulting from suppressing rigid body displacements. This matrix can be constructed by replacing $\boldsymbol{V}$ in the preceding equation by its *deformational* component $\widetilde{\boldsymbol{V}} \in \mathbb{R}^{M\times n-n^{rb}}$, i.e.:

$$\boldsymbol{K}^* := (\boldsymbol{\Psi}^T \widetilde{\boldsymbol{V}})^T \boldsymbol{H}^{-T} (\boldsymbol{\Phi}^T \boldsymbol{K}^{\boldsymbol{\mu}} \boldsymbol{\Phi}) \boldsymbol{H}^{-1} (\boldsymbol{\Psi}^T \widetilde{\boldsymbol{V}}) \tag{72}$$

(the deformational component of $\boldsymbol{V}$ is an orthogonal matrix such that $\texttt{cols}(\widetilde{\boldsymbol{V}}) \oplus \texttt{cols}(\boldsymbol{R}_{\boldsymbol{b}}) = \texttt{cols}(\boldsymbol{V})$, where $\texttt{cols}(\bullet)$ stands for the column space of its argument, and $\oplus$ symbolizes direct sum of subspaces).

Notice that $\boldsymbol{K}^{\boldsymbol{\mu}}$ is semi-positive definite, the zero eigenvalues being associated to the fine-scale rigid body modes. However, the deformational modes $\boldsymbol{\Phi}$ are by construction (see Eq. (2)) orthogonal to such rigid body modes, and therefore, $(\boldsymbol{\Phi}^T \boldsymbol{K}^{\boldsymbol{\mu}} \boldsymbol{\Phi})$ is positive definite. It follows then that $\boldsymbol{H}^{-T} (\boldsymbol{\Phi}^T \boldsymbol{K}^{\boldsymbol{\mu}} \boldsymbol{\Phi}) \boldsymbol{H}$ exhibits this property as well. Therefore, whether $\boldsymbol{K}^*$ is positive definite or not depends on the properties of the matrix $(\boldsymbol{\Psi}^T \widetilde{\boldsymbol{V}}) \in \mathbb{R}^{p\times n-n^{rb}}$, more specifically, for $\boldsymbol{K}^*$ to be positive definite, it can be shown that the *kernel* or nullspace of such matrix should only contain the zero vector

$$ker(\boldsymbol{\Psi}^T \widetilde{\boldsymbol{V}}) = \{\boldsymbol{0}\} \tag{73}$$

(the argument leading to this conclusion is similar to the one invoked when discussing the celebrated LBB condition in mixed finite elements, see e.g. Ref. [38], page 283).

Thus, we have to demonstrate that condition (70) implies the satisfaction of the preceding condition. To this end, firstly, notice that, according to proviso (70), $p \geq n - n^{rb}$. Hence, Eq. (73) can be equivalently formulated as

$$\texttt{rank}(\boldsymbol{\Psi}^T \widetilde{\boldsymbol{V}}) = n - n^{rb}. \tag{74}$$

Finally, by virtue of Eq. (9), it is readily seen that Eq. (70) does guarantee that the preceding equation is satisfied, as stated:

$$\texttt{rank}(\boldsymbol{\Psi}^T \boldsymbol{V}) = \texttt{rank}(\boldsymbol{\Psi}^T [\widetilde{\boldsymbol{V}}\ \mathbf{R}]) = \texttt{rank}(\boldsymbol{\Psi}^T \widetilde{\boldsymbol{V}}) = n - n^{rb}. \tag{75}$$

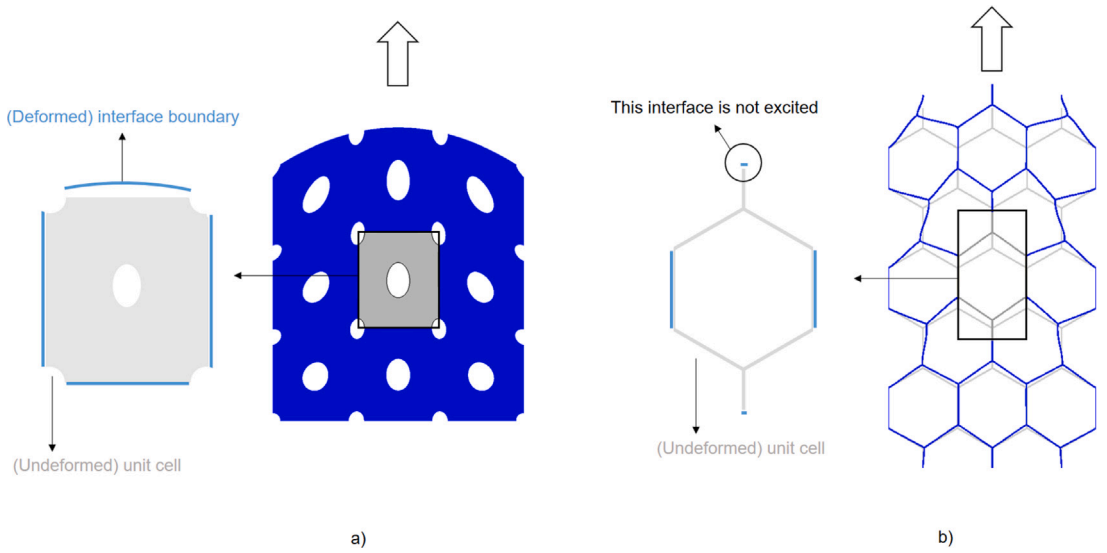

Fig. 21. Training test aimed at exciting the interface mode corresponding to the quadratic shape functions at the top midside node. (a) Porous domain. (b) Hexagonal cell. In the latter case, the prescribed displacement is not able to excite the mode, and as a consequence, stability condition (70) is not met.

A.2. Practical considerations

Loosely speaking, condition (70) is telling us that the self-equilibrated force modes $\boldsymbol{\Psi}$ obtained from the training tests should be such that they can excite any linear combination of interface modes $\boldsymbol{V}_1, \boldsymbol{V}_2, \ldots \boldsymbol{V}_n$ (except for rigid body modes). This is the reason why we emphasized in Section 2 that the solutions obtained in the *basic training tests* must be included in the training data, for each of one of such tests attempts to excite *one interface mode at a time*. Our findings indicate that the more continuous the interface boundary of the studied domain, the more effective the excitation of the interface modes, and therefore, the higher the probability that condition (70) is satisfied.

We illustrate this observation in Fig. 21 by displaying two extreme cases: one in which stability condition (70) is met, Fig. 21.a, and one in which it is not (Fig. 21.b). The former is the case of the porous domain shown in previous figures. The interface mode represents a parabolic vertical displacements of the top interface surface, with the maximum located at the midpoint; to excite this mode, we impose a similar displacement pattern on the top surface of the training domain. It can be appreciated that, despite being a discontinuous interface boundary, the degree of discontinuity is not severe and the displacement pattern is successfully transmitted to the top interface boundary of the central domain (from which we get the snapshots). By contrast, the hexagonal unit cell in Fig. 21.b has an ostensibly discontinuous interface boundary and, as a consequence, the parabolic displacement prescribed on the top is not able to induce a similar parabolic pattern on the top boundary interface (observe that this top boundary interface only represents a tiny portion of the top side of the rectangular element in which the cell is inscribed). In cases such as the hexagonal honeycomb cell shown in Fig. 21.b, the parameterization advocated by the first author for domain decomposition problems in Ref. [10], which is based on independent rigid body displacements for the 4 interface boundaries (enriched with empirical modes learned from the training experiments), would be more appropriate in this case.

To detect ill-conditioned problems such as the one shown in Fig. 21.b, it is recommended, when constructing the EIF operators of a given parent domain (in the offline stage), to compute and inspect all the singular values of $\boldsymbol{\Psi}^T\boldsymbol{V}$. Stable elements are characterized by smooth decays of such values, while unstable elements usually exhibits sharp drops in the smaller values (typically 2 or more orders of magnitude).

Appendix B. Determination of rotation matrices

In this appendix, we describe the procedure employed for identifying the parameters appearing in the coordinate transformation (56) (between the EIFE parent domain and the "physical" domain of a given EIF element). The input data for carrying out such identification are, on the one hand, the coordinates of the nodes of the EIF element (obtained from the corresponding coarse-scale mesh, see Fig. 7):

$$\boldsymbol{X} = \begin{bmatrix} \boldsymbol{x}_1 & \boldsymbol{x}_2 & \cdots & \boldsymbol{x}_{n^{nod}} \end{bmatrix}, \tag{76}$$

and, on the other hand, the coordinate matrix of the coarse-scale nodes of the EIF parent domain (the one used in the training process):

$$\boldsymbol{X}' = \begin{bmatrix} \boldsymbol{x}'_1 & \boldsymbol{x}'_2 & \cdots & \boldsymbol{x}'_{n^{nod}} \end{bmatrix}. \tag{77}$$

As pointed out in the introductory section, the preceding matrix may represent the location of nodes that do not coincide with any of the fine-scale nodes (recall that these are the nodes of a *fictitious frame* enclosing the fine-scale mesh, see Fig. 1). Besides, in order to ensure that the mapping does not introduce distortions, the criterion for positioning non-corner nodes in curved quadratic elements (or higher order) must be the same as the one employed by the mesh algorithm in constructing the coarse-scale mesh of the structure under study.

The particular order of the columns in Eq. (76) is dictated by the node connectivity information provided by the mesh algorithm. However, this particular order may not be compatible to the desired transformation. It is necessary, thus, to test all the permutations of the columns of $\boldsymbol{X}'$ that ensure mappings between parent and physical domains with positive Jacobians. The set of all such permutations will be denoted by $\boldsymbol{P} = \{\boldsymbol{P}_1, \boldsymbol{P}_2 \dots \boldsymbol{P}_{m^{per}}\}$. For linear quadrilateral, this list is obtained by cyclic permutations, i.e.: $\boldsymbol{P}_1 = [1,2,3,4]$, $\boldsymbol{P}_2 = [2,3,4,1]$, $\boldsymbol{P}_3 = [3,4,1,2]$ and $\boldsymbol{P}_4 = [4,1,2,3]$. For quadratic quadrilateral there are also $m^{per} = 4$ possible combinations, that can be obtained by cyclic permutation as well, in this case of both corner nodes and mid-side nodes. In the case of linear and quadratic hexahedral elements, the number of possible permutations raises to $m^{per} = 24$ (8 cyclic permutations per reference plane).

Let us calculate now, for a given $\boldsymbol{p} \in \boldsymbol{P}$, the parameters appearing in the coordinate transformation (56). The centroid $\boldsymbol{c}'$ and the translation vector $\boldsymbol{t}$ are given by $\boldsymbol{c}' = 1/n^{nod} \sum_{i=1}^{n^{nod}} \boldsymbol{x}'_i$ and $\boldsymbol{t} = 1/n^{nod} \sum_{i=1}^{n^{nod}} \boldsymbol{x}_i$. The scaling factor λ may be obtained as $\lambda = L/L'$, where L and L' are the maximum distances between consecutive points in matrices $\boldsymbol{X}'$ and $\boldsymbol{X}(\boldsymbol{p}, :)$, respectively (see also Fig. 7). Given $\boldsymbol{t}$, $\boldsymbol{c}'$ and λ, we can calculate the level of *straining* involved in the transformation, as a function of $\boldsymbol{Q}$ and $\boldsymbol{p}$, by computing the norm of the following matrix:

$$\boldsymbol{D}(\boldsymbol{p}, \boldsymbol{Q}) := \boldsymbol{Y}(\boldsymbol{p}) - \boldsymbol{Q}\boldsymbol{Z} \tag{78}$$

where

$$\boldsymbol{Y}(\boldsymbol{p}) := \begin{bmatrix} \boldsymbol{x}_{\boldsymbol{p}(1)} - \boldsymbol{t} & \boldsymbol{x}_{\boldsymbol{p}(2)} - \boldsymbol{t} & \cdots & \boldsymbol{x}_{\boldsymbol{p}(n^{nod})} - \boldsymbol{t} \end{bmatrix} \tag{79}$$

and

$$\boldsymbol{Z} := \lambda \begin{bmatrix} \boldsymbol{x}'_1 - \boldsymbol{c}' & \boldsymbol{x}'_2 - \boldsymbol{c}' & \cdots & \boldsymbol{x}'_{n^{nod}} - \boldsymbol{c}' \end{bmatrix} \tag{80}$$

We seek mappings involving pure rotation, without straining; this amounts to seek the rotation matrix $\boldsymbol{Q}$ and permutation $\boldsymbol{p}$ that minimize the norm of $\boldsymbol{D}$:

$$\begin{aligned} \min_{\boldsymbol{Q},\boldsymbol{p}} \quad & \|\boldsymbol{Y}(\boldsymbol{p}) - \boldsymbol{Q}\boldsymbol{Z}\|_F \\ \text{s.t.} \quad & \boldsymbol{Q}^T\boldsymbol{Q} = \boldsymbol{I} \\ & \boldsymbol{p} \in \boldsymbol{P} \end{aligned} \tag{81}$$

For a fixed $\boldsymbol{p}$, the solution of the above problem (which is known as a subspace rotation problem, see Ref. [25], page 327) is given by $\boldsymbol{Q} = \boldsymbol{U}_Q \boldsymbol{V}_Q^T$, where $\boldsymbol{U}_Q$ and $\boldsymbol{V}_Q$ are the left-singular and right-singular vectors of $\boldsymbol{Z}\boldsymbol{Y}^T$

$$[\boldsymbol{U}_q, \boldsymbol{S}_q, \boldsymbol{V}_q] \leftarrow \mathrm{SVD}(\boldsymbol{Z}\boldsymbol{Y}^T). \tag{82}$$

Let $\boldsymbol{Q}_i^*$ denote the solution of problem (81) for $\boldsymbol{p} = \boldsymbol{P}_i$, and $\gamma_i = \|\boldsymbol{D}(\boldsymbol{P}_i, \boldsymbol{Q}_i^*)\|_F$ the corresponding objective function ($i = 1, 2 \dots m^{per}$). In searching for the final solution of the problem, one may encounter three different scenarios, namely:

1. There is just one admissible solution, that is, there is just one i such that $\gamma_i = 0$. This is the case, for instance, when dealing with curved elements.
2. There are multiplicity of solutions ($\gamma_i = 0$ for several indexes i). This is the case encountered when dealing with symmetric elements such as the square shown previously in Fig. 7. In this scenario, the user is to provide further information of which configuration to choose (for instance, in the domain displayed in Fig. 7, which contains an elliptical inclusion, one has to specify how to orient the ellipse in each coarse-scale element).
3. The last possible scenario is when $\gamma_i \neq 0$ for all i, that is, when apparently there is no solution, because all possible transformation involves straining. This implies that the fine-scale mesh assigned to the coarse-scale element does not "fit" into the element unless some straining is introduced. Small straining levels may be tolerated (typically $\gamma_i/n^{nod} \leq 10^{-3}$); for higher levels, it is necessary to train the domain with this new shape, and obtain new set of deformational and self-equilibrated modes.

References

[1] M.G. Geers, V.G. Kouznetsova, K. Matous, J. Yvonnet, Homogenization methods and multiscale modeling: nonlinear problems, in: Encyclopedia of Computational Mechanics Second Edition, Wiley Online Library, 2017, pp. 1–34.

[2] Y. Efendiev, T.Y. Hou, Multiscale Finite Element Methods: Theory and Applications, Vol. 4, Springer Science & Business Media, 2009.

[3] F. Feyel, J.L. Chaboche, FE2 multiscale approach for modelling the elastoviscoplastic behaviour of long fibre SiC/Ti composite materials, Comput. Methods Appl. Mech. Engrg. 183 (3–4) (2000) 309–330.

[4] J.A. Hernández, J. Oliver, A.E. Huespe, M. Caicedo, J. Cante, High-performance model reduction techniques in computational multiscale homogenization, Comput. Methods Appl. Mech. Engrg. 276 (2014) 149–189.

[5] J. Oliver, M. Caicedo, A.E. Huespe, J.A. Hernández, E. Roubin, Reduced order modeling strategies for computational multiscale fracture, Comput. Methods Appl. Mech. Engrg. 313 (2017) 560–595.

[6] M. Caicedo, J.L. Mroginski, S. Toro, M. Raschi, A. Huespe, J. Oliver, High performance reduced order modeling techniques based on optimal energy quadrature: application to geometrically non-linear multiscale inelastic material modeling, Arch. Comput. Methods Eng. 26 (2019) 771–792.
[7] M. Raschi, O. Lloberas-Valls, A. Huespe, J. Oliver, High performance reduction technique for multiscale finite element modeling (HPR-FE2): Towards industrial multiscale FE software, Comput. Methods Appl. Mech. Engrg. 375 (2021) 113580.
[8] J.A. Hernandez, J.R. Bravo, S.A. de Parga, CECM: A continuous empirical cubature method with application to the dimensional hyperreduction of parameterized finite element models, 2023, arXiv:2308.03877.
[9] J.A. Hernández, M.A. Caicedo, A. Ferrer, Dimensional hyper-reduction of nonlinear finite element models via empirical cubature, Comput. Methods Appl. Mech. Engrg. 313 (2017) 687–722.
[10] J.A. Hernández, A multiscale method for periodic structures using domain decomposition and ECM-hyperreduction, Comput. Methods Appl. Mech. Engrg. 368 (2020) 113192.
[11] A.T. Patera, M. Yano, An LP empirical quadrature procedure for parametrized functions, C. R. Math. 355 (11) (2017) 1161–1167.
[12] M. Yano, A.T. Patera, An LP empirical quadrature procedure for reduced basis treatment of parametrized nonlinear PDEs, Comput. Methods Appl. Mech. Engrg. 344 (2019) 1104–1123.
[13] M. Yano, Discontinuous Galerkin reduced basis empirical quadrature procedure for model reduction of parametrized nonlinear conservation laws, Adv. Comput. Math. 45 (2019) 2287–2320.
[14] C. Farhat, P. Avery, T. Chapman, J. Cortial, Dimensional reduction of nonlinear finite element dynamic models with finite rotations and energy-based mesh sampling and weighting for computational efficiency, Internat. J. Numer. Methods Engrg. 98 (9) (2014) 625–662.
[15] A. Giuliodori, J.A. Hernández, E. Soudah, Multiscale modeling of prismatic heterogeneous structures based on a localized hyperreduced-order method, Comput. Methods Appl. Mech. Engrg. 407 (2023) 115913.
[16] K. Park, C.A. Felippa, A variational principle for the formulation of partitioned structural systems, Internat. J. Numer. Methods Engrg. 47 (1–3) (2000) 395–418.
[17] Y. Efendiev, J. Galvis, T.Y. Hou, Generalized multiscale finite element methods (GMsFEM), J. Comput. Phys. 251 (2013) 116–135.
[18] T.Y. Hou, X.H. Wu, A multiscale finite element method for elliptic problems in composite materials and porous media, J. Comput. Phys. 134 (1) (1997) 169–189.
[19] Y.R. Efendiev, T.Y. Hou, X.H. Wu, Convergence of a nonconforming multiscale finite element method, SIAM J. Numer. Anal. 37 (3) (2000) 888–910, http://dx.doi.org/10.1137/S0036142997330329.
[20] N.C. Nguyen, A multiscale reduced-basis method for parametrized elliptic partial differential equations with multiple scales, J. Comput. Phys. 227 (23) (2008) 9807–9822.
[21] Y. Efendiev, J. Galvis, X.H. Wu, Multiscale finite element methods for high-contrast problems using local spectral basis functions, J. Comput. Phys. 230 (4) (2011) 937–955.
[22] P. Diercks, K. Veroy, A. Robens-Radermacher, J.F. Unger, Multiscale modeling of linear elastic heterogeneous structures based on a localized model order reduction approach, 2022, arXiv preprint arXiv:2201.10374.
[23] T.J. Hughes, G.R. Feijóo, L. Mazzei, J.B. Quincy, The variational multiscale method—a paradigm for computational mechanics, Comput. Methods Appl. Mech. Engrg. 166 (1–2) (1998) 3–24.
[24] C. Miehe, A. Koch, Computational micro-to-macro transitions of discretized microstructures undergoing small strains, Arch. Appl. Mech. 72 (2002) 300–317.
[25] G.H. Golub, C.F. Van Loan, Matrix Computations, JHU Press, 2013.
[26] G.H. Silva, R. Le Riche, J. Molimard, A. Vautrin, Exact and efficient interpolation using finite elements shape functions, Eur. J. Comput. Mech. 18 (3–4) (2009) 307–331.
[27] T. Hughes, The Finite Element Method: Linear Static and Dynamic Finite Element Analysis, Vol. 682, Dover Publications New York, 2000.
[28] M. Elad, Sparse and Redundant Representations: From Theory to Applications in Signal and Image Processing, Vol. 2, No. 1, Springer, 2010.
[29] T. Belytschko, W.K. Liu, B. Moran, K. Elkhodary, Nonlinear Finite Elements for Continua and Structures, John wiley & sons, 2014.
[30] M.G. Geers, V.G. Kouznetsova, W. Brekelmans, Multi-scale computational homogenization: Trends and challenges, J. Comput. Appl. Math. 234 (7) (2010) 2175–2182.
[31] J.C. Simo, T.J. Hughes, Computational Inelasticity, Vol. 7, Springer Science & Business Media, 2006.
[32] J.C. Simo, T.J.R. Hughes, Computational Inelasticity, Springer, New York, 1998.
[33] D. Amsallem, M.J. Zahr, K. Washabaugh, Fast local reduced basis updates for the efficient reduction of nonlinear systems with hyper-reduction, Adv. Comput. Math. 41 (5) (2015) 1187–1230.
[34] S. Grimberg, C. Farhat, R. Tezaur, C. Bou-Mosleh, Mesh sampling and weighting for the hyperreduction of nonlinear Petrov-Galerkin reduced-order models with local reduced-order bases, Internat. J. Numer. Methods Engrg. (2020).
[35] J. Barnett, C. Farhat, Quadratic approximation manifold for mitigating the Kolmogorov barrier in nonlinear projection-based model order reduction, J. Comput. Phys. 464 (2022) 111348.
[36] J.B. Rutzmoser, D.J. Rixen, P. Tiso, S. Jain, Generalization of quadratic manifolds for reduced order modeling of nonlinear structural dynamics, Comput. Struct. 192 (2017) 196–209.
[37] K. Lee, K.T. Carlberg, Model reduction of dynamical systems on nonlinear manifolds using deep convolutional autoencoders, J. Comput. Phys. (2019) 108973.
[38] J. Donea, A. Huerta, Finite Element Methods for Flow Problems, John Wiley & Sons, 2003.